Article

Diverse genesis of early Earth's continental crust hints the geodynamic transition at about 3.0 Gyrs ago

Check for updates

Hairuo Wang[1,2,3], Keda Cai[1,2,3] ✉, Min Sun[4], Wei-Ran Li [4], Ming Chen[5,6] & Xiao-Ping Xia [7,8]

Tonalite-trondhjemite-granodiorite suites, dominating Earth's early continental crust, likely formed by partial melting of hydrated metabasalt, but the specific conditions and mechanisms remain poorly constrained. Here, we conduct thermodynamic-geochemical modeling to systematically compare the roles that pressure, bulk H_2O content, and source rock composition play in shaping these ancient rocks. Accordingly, we assess their optimal forming conditions, which are further validated by magmatic H_2O contents retrieved from the apatite and zircon crystals of tonalite-trondhjemite-granodiorite suites. Our results highlight that pressure is the first-order factor controlling the formation and compositional diversity of these rock suites. Those with "high-pressure" geochemical characteristics are derived from fluid-fluxed melting at 14 – 16 kbar, a process readily explained by subduction rather than intraplate geodynamic regime. Furthermore, the temporal and spatial distributions of "high-pressure" variants, coupled with those of arc-like basalts, suggest subduction that likely initiated as a local phenomenon and transitioned to a global-scale process by 3.0 Ga.

The nuclei of the Archean cratons are mainly composed of low-potassium (K) felsic intrusive rocks of the tonalite-trondhjemite-granodiorite (TTG) suite, which represents the main constituent of early continental crust[1–4]. Clarifying how these rocks formed is fundamental to understanding the origin and stabilization of continental crust. TTGs, primarily occurring as variably deformed and metamorphosed gneisses, are generally accepted to have originated from partial melting of hydrated metabasalt[1,2,5–7]. They are typically rich in sodium (Na) but depleted in heavy rare earth elements (HREE), niobium (Nb), and tantalum (Ta), relative to potassic granitoids[8]. On top of these common characteristics, TTGs exhibit compositional diversity primarily in trace element signatures (e.g., Sr/Y and Nb/Ta ratios)[1,2,8,9]. Despite some TTGs show the influence of fractional crystallization[10–12], the compositional diversity of most TTGs was interpreted to be caused by variable mineral assemblages (e.g., garnet, amphibole, rutile, and plagioclase) in the solid residue during partial melting[3,6,13]. This interpretation is based on the general absence of cumulates formed by fractional crystallization in geological records of the early Earth[2]. However, the melting reaction of Archean metabasalt to form TTG magmas depends on multiple factors, including temperature (T), pressure (P), bulk H_2O

content (X_{H_2O}), and source rock composition[6,9,14]. The interplay between these factors has led to the proposal of multiple hypotheses to interpret the forming conditions and processes of TTGs, sparking considerable controversy surrounding the geodynamic setting of the early Earth.

Previous experimental studies based on fluid-absent melting of MORB-like metabasalt proposed that TTG chemical variability is probably derived from partial melting of mafic proto-crust at different depths, which can modulate melt trace element composition through controlling the proportions of pressure-sensitive minerals in the residue, primarily plagioclase (rich in Sr), garnet (rich in HREE), and rutile (rich in Nb)[5,15–17]. Accordingly, TTGs have been classified into variants defined by geochemical characteristics indicative of low-pressure ("LP"), medium-pressure ("MP"), and high-pressure ("HP") conditions[1,8]. As the most controversial end-member, "HP"-TTGs have the highest Sr/Y ratio but the lowest Nb/Ta ratio and HREE content, interpreted to be extracted from a garnet-amphibolite or eclogite residue at ~15–20 kbar[5,6,8,18,19]. They are endowed with tectonic significance, prompting the proposal of various geodynamic models for the early Earth, which involve both subduction (plate tectonics model)[15,18] and non-subduction scenarios (e.g., stagnant-lid,

[1]State Key Laboratory of Geological Processes and Mineral Resources, China University of Geosciences (Beijing), Beijing, China. [2]Frontiers Science Center for Deep-time Digital Earth, China University of Geosciences (Beijing), Beijing, China. [3]School of Earth Sciences and Resources, China University of Geosciences (Beijing), Beijing, China. [4]Department of Earth and Planetary Sciences, The University of Hong Kong, Hong Kong, China. [5]State Key Laboratory of Geological Processes and Mineral Resources, China University of Geosciences, Wuhan, China. [6]School of Earth Sciences, China University of Geosciences, Wuhan, China. [7]Hubei Key Laboratory of Petroleum Geochemistry and Environment, Yangtze University, Wuhan, China. [8]College of Resources and Environment, Yangtze University, Wuhan, China. ✉e-mail: caikd@cugb.edu.cn

1

mantle plume, sagduction, and dripping models)[20,21]. However, besides pressure, source rock composition has also been highlighted as a key control on the stability of garnet and thereby TTG magma compositions. The stability field of garnet can be substantially extended to a low-pressure region (~7 kbar) in the low Mg# (100 ×atomic Mg/(Mg +Fe) of ~35) basaltic system, allowing "HP"-TTGs to form through partial melting at lower-crustal depths, without the requirement of subduction[9]. These high-Fe basalts, however, have markedly different compositions from most Archean metabasites preserved in greenstone belts, indicating that they are not universally representative[22,23]. Furthermore, recent works suggested that the capacity of amphibole to incorporate HREE and Nb allows it to substitute garnet and rutile, imparting the "high-pressure" characteristics (especially high Sr/Y) to magmas through low-pressure fluid-fluxed melting[24,25].

Given the critical roles that pressure, source rock composition, and bulk H_2O content play in controlling TTG magma compositions, evaluating the contribution of each factor is fundamental to accurately defining the forming condition of TTGs, consequently supporting a convincing basis for assessing the geodynamic background of the early Earth. However, most experimental and thermodynamic modeling studies focused only on a subset of variables, especially pressure and bulk H_2O content[13,14,26,27], and thus a comprehensive analysis of all controlling factors is warranted. While Palin et al.[6] provided a comprehensive assessment of these variables and the forming conditions for TTGs, their study was confined to H_2O-undersaturated to minimally H_2O-saturated melting, leaving the role of H_2O-fluxed melting and the range of bulk H_2O contents for TTG formation unaddressed. More importantly, the validation of results from experimental and modeling studies typically relies on a comparison of major and trace element compositions within TTG rocks, yet these signatures may be biased by differentiation processes during the storage and ascent of magma and/or long-term, complex metamorphism[28]. Beyond compositional constraints, other critical magma properties, particularly the H_2O content, are often overlooked[29]. On modern Earth, arc magmas generated at subduction zones are generally H_2O-rich, primarily due to the influx of fluids released from subducting oceanic plates[30], indicating that magmatic H_2O content can partly reflect the tectonic setting. Recent studies emphasized that accessory minerals such as zircon and apatite are to some extent resistant to metamorphism and may record the volatile contents of the magma from which they crystallized[31,32]. Specifically, Ge et al.[29] introduced a zircon oxybarometer-hygrometer to estimate the H_2O contents of Archean granitoids. However, zircon was questioned for only recording evolved magma information due to its low saturation temperature[33]. Unlike zircon, apatite incorporates halogens (F, Cl) in addition to OH^-[34], can have a higher crystallization temperature, and is commonly found in zircon as a crystal inclusion[35]. These allow apatite to record H_2O contents of less evolved magmas better than zircon, and offer new insights into the TTG formation and its geodynamic implications.

In this study, we conducted thermodynamic-geochemical modeling with a controlled variable approach to systematically compare the effects of pressure, bulk H_2O content, and source rock composition on the melting reaction of Archean metabasalt to form TTGs. We used the model results to infer the optimal forming conditions of TTGs and testified these using magmatic H_2O contents calculated independently from apatite (in this study) and zircon[29] of a large, global-scale dataset for TTGs. Our findings provide new insights into the potential tectonic regime of the early Earth.

Results and discussion
It is generally agreed that Archean TTGs were generated by partial melting of hydrated mafic rocks. While an assimilation-fractional crystallization origin was suggested for certain TTG rocks (e.g., Paleoarchean TTGs from Kaapvaal Craton[11] and Neoarchean TTGs from North China Craton[10]), there is a lack of evidence in most Archean TTGs, due to the rarity or absence of both intermediate products (e.g., diorite) and cumulates (e.g., garnetite) of fractional crystallization in Archean geological records[2]. Additionally, the compositional distribution of global TTGs shows the

limited impact of fractional crystallization on TTG compositions, as differentiation proxies (e.g., $MgO+Fe_2O_3$ content) show no systematic evolutionary trend among TTGs of similar ages within individual cratons (Supplementary Fig. 6). Moreover, these proxies show little temporal variation within each TTG type, with "LP"-TTGs consistently showing higher $MgO+Fe_2O_3$ contents than "HP"-TTGs (Supplementary Fig. 7). If "HP"-TTGs formed by fractional crystallization of "LP"-TTG melts, the shallow-derived "LP"-TTG melts would need to be transported into high-pressure regimes to satisfy the requirement of ~20% garnet fractionation (Fig. 1), which appears implausible. Hence, we consider partial melting of Archean basalts as the main mechanism to form Archean TTGs, and we carry out thermodynamic modeling described as follows.

Controlling factors of TTG compositions: pressure dominates over source rock composition and bulk H_2O content
We compare the effects of pressure and bulk H_2O content on melt composition by conducting 15 sets of closed-system isobaric melting modeling at pressures between 8 and 20 kbar, and seven calculations within each set (i.e., at a given pressure) using different bulk H_2O contents (1–4 wt.%) (Supplementary Table 1). While open-system fractional melting more realistically reflects melt extraction due to its low density, previous studies demonstrated that this exerts little effect on its major and trace elements compositions[36,37] (Supplementary Fig. 9), allowing melting to be approximated as a closed-system process. The source rock of all 105 runs was chosen to be an enriched Archean basalt[27], which is the most likely protolith for TTGs and accounts for their incompatible large-ion lithophile elements enrichment[6,27]. Notably, to better assess the compositional difference between the predicted melts and global Archean TTGs, we consider not only regular geochemical proxies (e.g., Sr/Y, Nb/Ta), but also a full set of REEs based on the λ shape coefficients[38]. The quantitative description of chondrite-normalized REE pattern shapes using these coefficients (λ_0 for abundance; λ_1 for slope; λ_2 for curvature) was suggested to be substantially
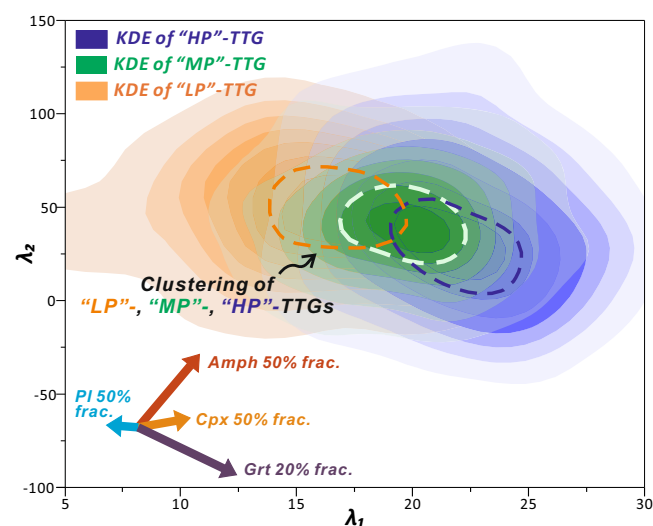

Fig. 1 | Compositional distribution of global Archean TTGs. The compositional variations of Archean TTGs, represented by λ shape coefficients[38] (λ_1, λ_2), are visualized using kernel density estimations (KDEs). λ shape coefficients are quantitative descriptions of chondrite-normalized REE pattern shapes, where λ_1 and λ_2 represent the slope and curvature of the REE pattern, respectively (see **Methods**). The areas outlined by dashed lines represent the data clustering regions of three TTG types, with a density exceeding 70%. The classification scheme of TTGs is provided in **Methods**. Although there is an obvious overlap between "MP"-TTGs and the other two types of TTGs, the boundary between "LP"- and "HP"-TTGs is relatively clear. The vectors in the lower left, calculated based on both Rayleigh fractionation and batch melting models, represent the impact of fractionation of different minerals (plagioclase, amphibole, clinopyroxene, and garnet), where their lengths correspond to the degree of fractionation. The transition from "LP"- to "HP"-TTGs exhibits pronounced control of garnet fractionation.
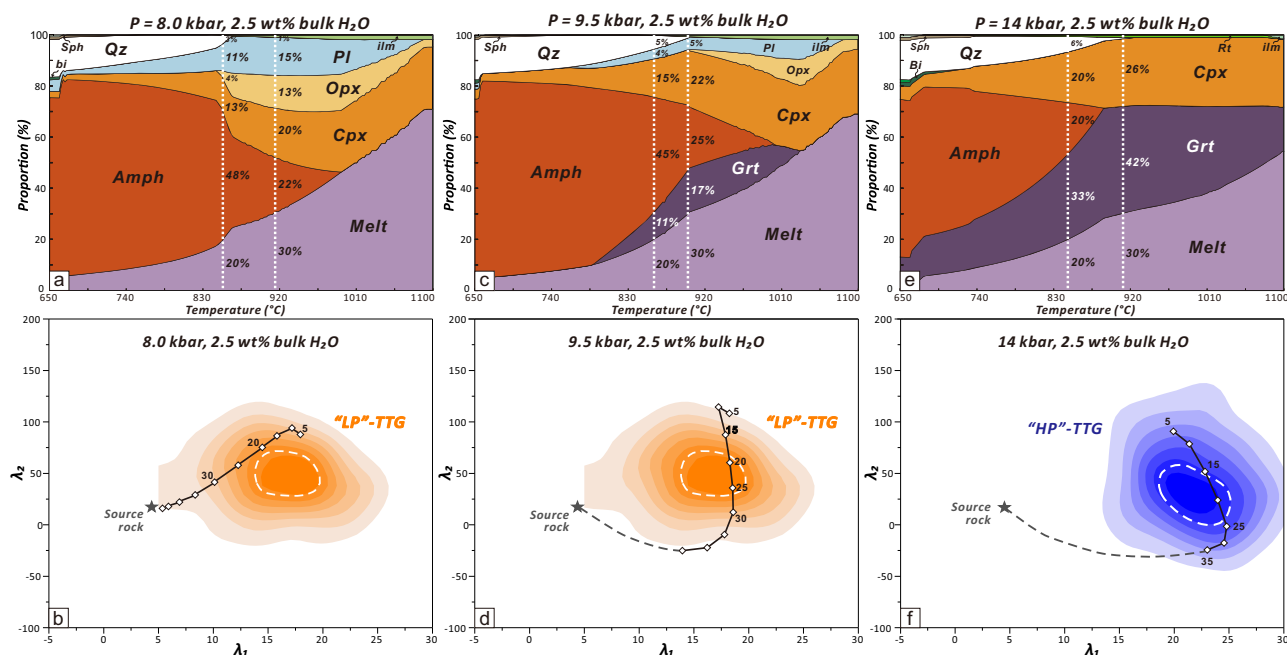
Fig. 2 | Calculated proportions of phases and geochemical modeling for specified melting cases. a, b Calculated phases proportions and melt composition for melting of median enriched Archean basalt[27] at 8.0 kbar and 2.5 wt.% bulk H_2O. **c, d** Calculated phases proportions and melt composition for melting of median enriched Archean basalt[27] at 9.5 kbar and 2.5 wt.% bulk H_2O. **e, f** Calculated phases proportions and melt composition for melting of median enriched Archean basalt[27] at 14 kbar and 2.5 wt.% bulk H_2O. The specific phase proportions at 20% and 30% partial melting are listed along the white dotted lines. The numbers around the nodes

for modeled melt compositions represent the degrees of partial melting. The calculated melt fractions are from 5 to 50% at 5% intervals. The white dashed lines outline the ranges of data density ≥70% (based on kernel density estimations), which represent the reference compositional range of each TTG type. In cases where amphibole is present in abundance within the solid residue but garnet is absent, the composition of the corresponding melt deviates from the compositional range of "LP"-TTGs. Only with a gradual increase of garnet within the residue does the composition of the melt evolve gradually from "LP"- to "HP"-TTGs.

more robust than conventional element ratios for petrogenetic analysis[39,40]. The thermodynamic modeling was carried out with the software GeoPS[41] and details of the calculations are provided in **Methods**.

For all modeling cases in this study, partial melting in amphibolite facies occurs only at low pressures (8 kbar with 1–4 wt.% H_2O and 8.5 kbar with 1–2.5 wt.% H_2O), with no garnet present in the solid residue. However, the compositions of the corresponding melts deviate significantly from those of TTGs, exhibiting higher λ_2 but lower λ_1 (Fig. 2a, b). Only as the proportion of garnet rises (garnet-amphibolite facies) does the predicted melt fall within the compositional range of "LP"-TTGs (Fig. 2c, d). Further increase in the proportion of garnet (garnet-pyroxenite facies) drives the melt toward "HP"-TTG region (Fig. 2e, f). These modeling results highlight garnet as the critical control on TTG types, as further supported by global TTG compositions where garnet fractionation is more pronounced during "HP"-TTG formation than in "LP"-TTGs (Fig. 1). We further investigated the stability field of garnet based on the thermodynamic model results and found that it can be affected by both pressure and bulk H_2O contents as detailed below.

In the low-pressure cases, an increase in bulk H_2O content expands the stability field of garnet, with its maximal modal amount achieved at 3–4 wt.% bulk H_2O and 830–960 °C (corresponding to ~20–30% partial melting) (Fig. 3a). This leads to melts derived from higher bulk H_2O contents characterized by more intense garnet fractionation. For instance, at 8.5 kbar and 30% partial melting, as bulk H_2O content increases from 1 wt.% to ≥3 wt.% the proportion of garnet in the solid residue rises from 0 to 5 wt.%, leading to a gradual increase in Sr/Y ratios and λ_1, and a decrease in λ_2 of the melt (Fig. 3). Similar shifts in garnet stability field were also observed by experimental work and attributed to the peritectic reaction of amphibole at low-pressure and H_2O-enriched conditions (amphibole + plagioclase + melt₁ → garnet + melt₂)[42]. However, our model results show that at higher pressures (≥9.5 kbar), changes in bulk H_2O contents have an opposite impact on the melting reaction, where the modal amount of garnet

is maximized at low bulk H_2O contents (<2 wt.%) (Fig. 4a). For example, at 11 kbar and 20% partial melting, the solid residue can contain the highest proportion of garnet with 1–1.5 wt.% bulk H_2O, resulting in the melt having the highest λ_1 but the lowest λ_2, whereas the presence of plagioclase leads to the lowest Sr/Y ratio (Fig. 4). As bulk H_2O content increases, the reduction in the proportion of garnet is accompanied by consumption of clinopyroxene but growth/crystallization of amphibole (Fig. 4b, c), aligned with the peritectic relationship between garnet and amphibole suggested by previous experimental work (garnet + clinopyroxene + melt → amphibole)[42]. Although H_2O content can influence the melt composition by controlling the transitions between amphibole and garnet, its impact is limited since compositional variations in the predicted melts are unlikely to exceed the range of a specific type of TTG (Figs. 3 and 4). Instead, pressure exerts substantial control over the stability of garnet, and accordingly, the composition of the melt. With the degree of partial melting between 20 and 30%, enhancing pressure from 9 kbar to 15 kbar causes the proportion of garnet in the solid residue to increase by 8 to 9 times, along with a rapid increase in Sr/Y and λ_1, and a decline in λ_2 of the melt, i.e., shifting from the "LP"-TTGs to the "HP"-TTGs field (Fig. 5). Moreover, increasing pressure also leads to a continuous rise in the proportion of rutile (up to ~1 wt.% at 15 kbar), causing a gradual decrease in the melt Nb/Ta ratio (Fig. 5d, h). This change cannot be achieved by merely altering the bulk H_2O content within the range of 1–4 wt.% (Supplementary Fig. 13).

Beyond pressure and bulk H_2O content, the stability of garnet is also highly sensitive to source rock Mg#[9]. To assess its effect on TTG formation, three more modeling sets were added for the three types of TTGs, where melting conditions (P-X_{H_2O}) were set to be the same as the best fit obtained from the above modeling, i.e., "LP" (9 kbar, 1.5 wt.% H_2O), "MP" (11 kbar, 2.5 wt.% H_2O), and "HP" (15 kbar, 3.5 wt.% H_2O), respectively (Fig. 6). Each set includes eight calculations where the source rock Mg# was increased from 41 to 45 for Archean basalts, to higher values of 76–80 (see **Methods**). Notably, basalts of similar Mg# exhibit comparable major (e.g., CaO, Na_2O,
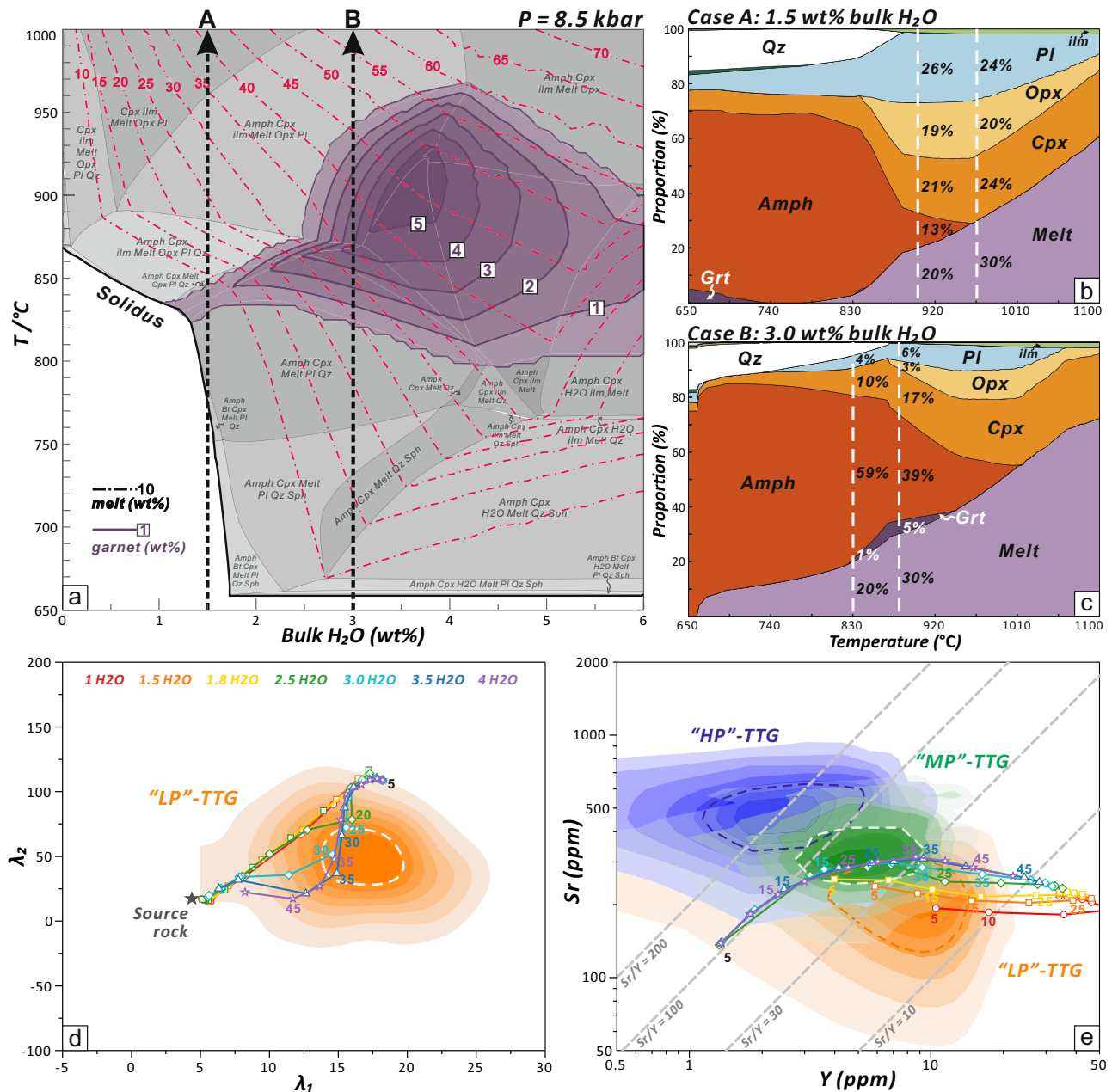
Fig. 3 | Thermodynamic-geochemical modeling of isobaric melting at 8.5 kbar. **a** Simplified T-X_{H_2O} pseudosection for median enriched Archean basalt[27] at 8.5 kbar, with contours showing calculated modal proportions of garnet (purple-colored field and purple lines) and melt fraction (pink dashed lines). The two bold, dashed lines with arrows represent melting cases with bulk H_2O contents of 1.5 wt.% (case A) and 3 wt.% (case B), respectively. **b, c** Calculated modal mineral and melt proportions versus temperature for case A and case B, respectively. The specific proportions of each phase at 20% and 30% partial melting are listed along the white dashed lines. **d, e** Compositional comparisons (λ_1 versus λ_2, Sr versus Y) between modeling melts and TTGs. Not only the 1.5 and 3.0 wt.% bulk H_2O cases but also the melts for cases of other bulk H_2O content are taken into account. Different colors refer to different bulk H_2O content, and the numbers around the nodes represent the degree of partial melting. The calculated melt fractions are from 5 to 50% at 5% intervals.

K_2O, Al_2O_3) and trace element (e.g., Nb/Ta and Sr/Y ratios, λ shape coefficients) compositions (Supplementary Fig. 17). Moreover, only the abundances of REEs exhibit significant differences between basalts of different Mg# (λ_0 decreases with increasing Mg#), but they only affect the λ_0 values of the modeled melts. These comparisons imply that the control of source rock compositions mainly derives from the variation in Mg#.

For high-pressure cases (11 & 15 kbar), the results show that at equivalent partial melting degree, the mineral assemblages of solid residue are comparable across runs within the same set, giving a compositional similarity in corresponding melts (Fig. 6e–h and Supplementary Fig. 15). These demonstrate that source rock composition exerts a rather small

control over the melting reactions at relatively high pressures. The modeling from the low-pressure set (9 kbar), however, reveals more complex patterns. At 30% partial melting, lowering the source rock Mg# from 76–80 to 41–45 causes the garnet proportion to increase by 20 wt.%, shifting the melting reaction from amphibolite- to garnet-amphibolite facies, thereby increasing melt λ_1 and Sr/Y, and decreasing melt λ_2 and Nb/Ta (Fig. 6a–d). Although the source rock composition shows a greater control over the melting reaction at low pressures than high pressures, only the melts of the lowest Mg# (41-45) align with the observed "MP"-TTGs composition, whereas the rest disperse within the "LP"-TTGs region (Fig. 6a–c). Notably, the hot mantle in the early Earth was suggested to undergo a high degree of partial
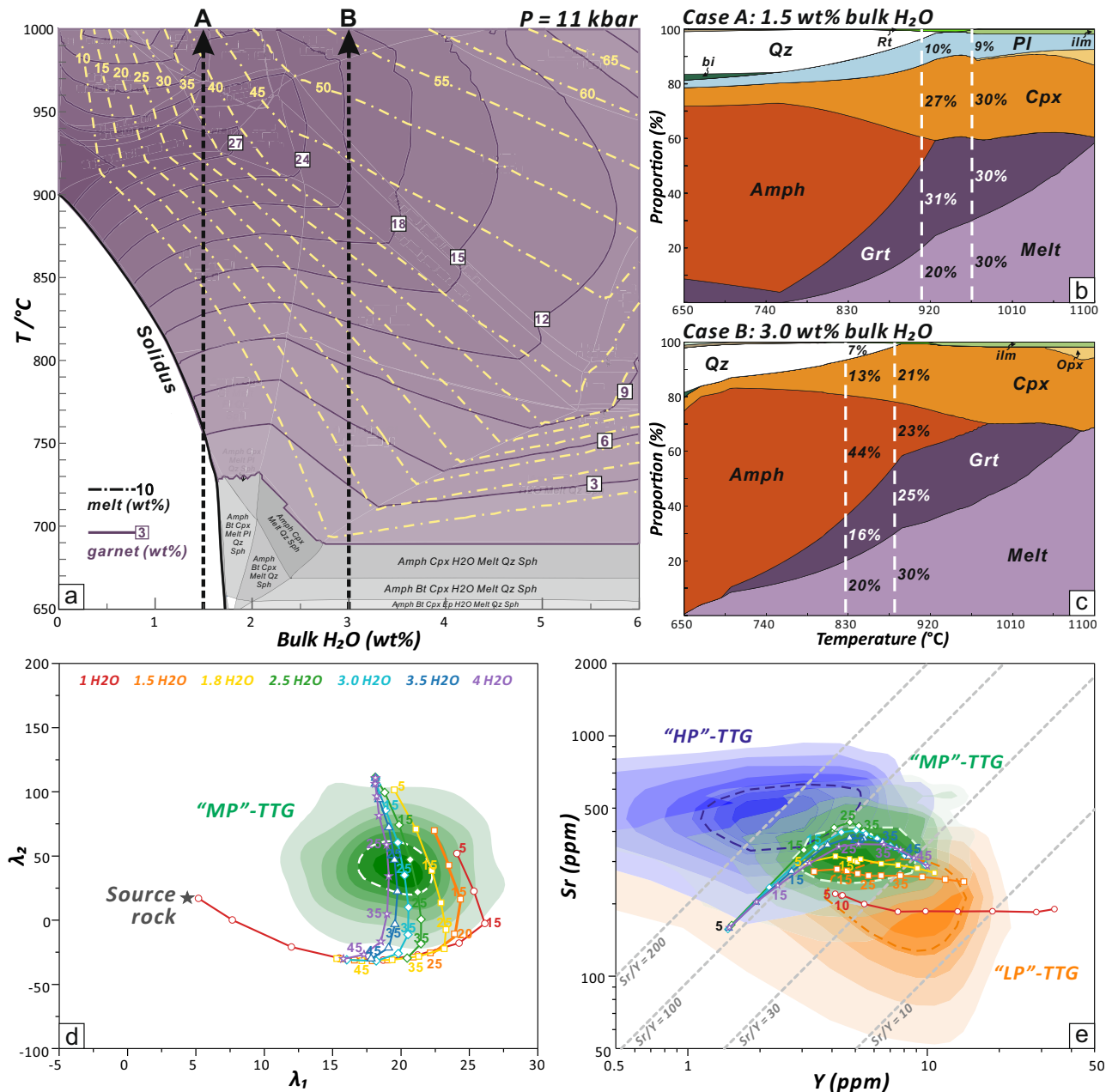
Fig. 4 | Thermodynamic-geochemical modeling of isobaric melting at 11 kbar.
a Simplified T-X_{H_2O} pseudosection for median enriched Archean basalt[27] at 11 kbar, with contours delineating the proportions of garnet (purple-colored field and purple lines) and melt fraction (light-yellow dashed lines). The two bolded, dashed lines with arrows represent melting cases with bulk H_2O contents of 1.5 wt.% (case A) and 3 wt.% (case B), respectively. **b**, **c** Mineral and melt proportions versus temperature for case A and case B, respectively, with the phase proportions at 20% and 30% partial melting highlighted along the white dashed lines. **d**, **e** Compositional comparisons (λ_1 versus λ_2, Sr versus Y) between modeling melts and TTGs, incorporating not just the 1.5 and 3.0 wt.% bulk H_2O cases but also those with different H_2O contents. Colors represent varying bulk H_2O contents, and the numbers around the nodes correspond to the degree of partial melting. The calculated melt fractions are from 5 to 50% at 5% intervals. At a fixed pressure, the change in the composition of the modeling melt caused by the variation in bulk H_2O content (from 1 to 4 wt.%) is minor.

melting on decompression, resulting in Archean oceanic crust with Mg# of ~60 (ref. 22). The source rocks with Mg# <45 from our models only account for less than 5% of global Archean basalts (Supplementary Fig. 16) and are all enriched in incompatible trace elements, possibly due to localized modification of the proto-mafic crust[43,44]. Thus, from the global Archean basalt perspective, the influence of source rock composition on TTG melts appears minor.

Integrating all model results, we conclude that pressure is the first-order controlling factor of the formation of different types of TTGs, which is in line with previous experimental[14,16] and thermodynamic studies[6,27]. In addition, variations in source rock composition and bulk H_2O content may contribute to the compositional dispersion observed within each type of Archean TTG.

Defining the optimal melting conditions for Archean TTGs formation

Alongside the above-mentioned investigation of the key variables for TTGs formation, we assess the melting conditions (P-T-X_{H_2O}) required for generating the three types of TTGs from proto-mafic crust. The major and trace elements compositions of the calculated partial melts best match natural
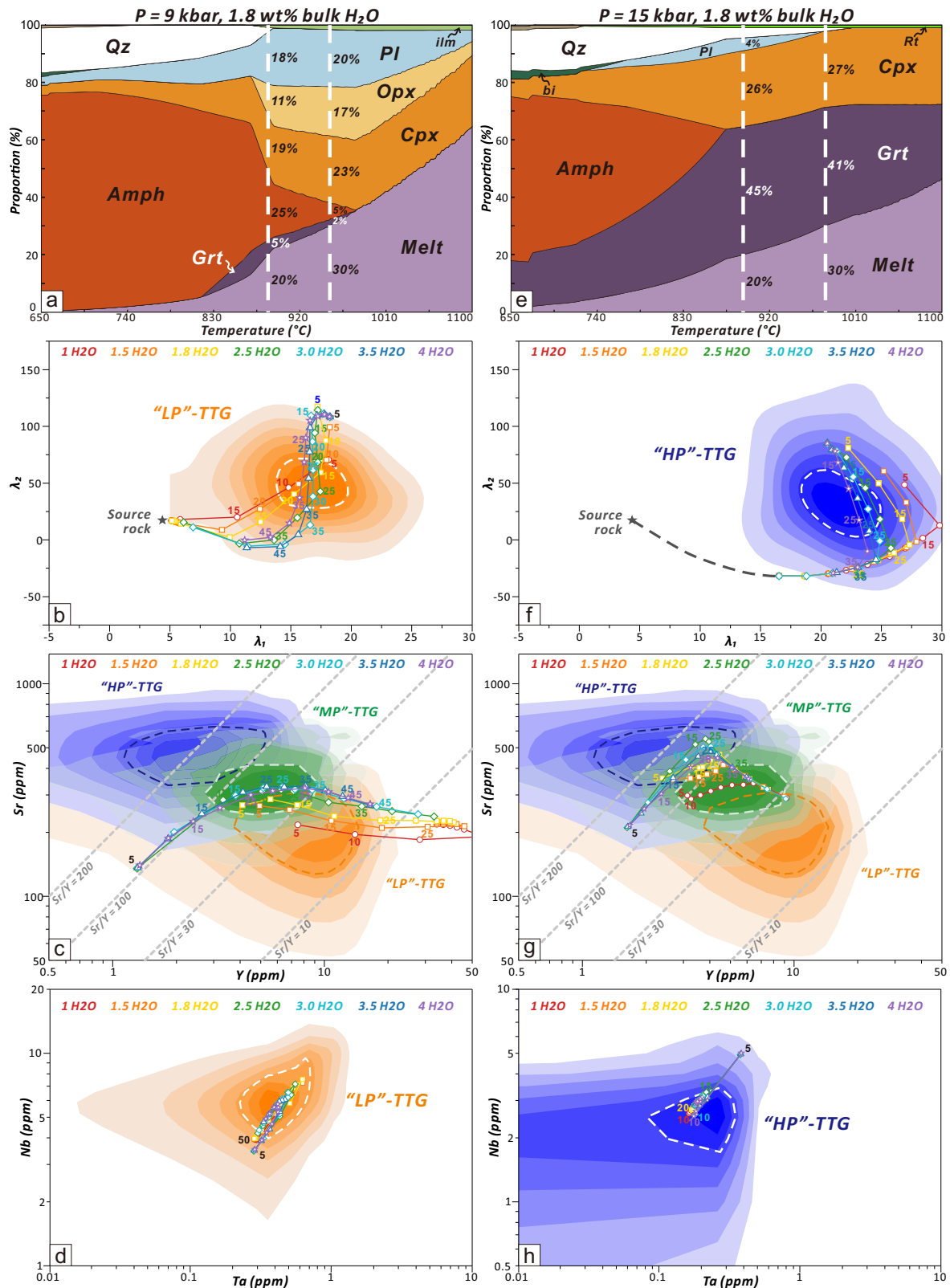
Fig. 5 | Calculated proportions of phases and geochemical modeling for low-pressure and high-pressure melting cases. The left column shows the results of partial melting at 9 kbar, while the right column shows those of partial melting at 15 kbar. The source rock is set as median enriched Archean basalt[27]. **a, e** Calculated modal proportion of minerals and melts for melting at 1.8 wt.% bulk H_2O content but at different pressures. As the pressure increases, the proportion of garnet at the same degree of partial melting rises rapidly. **b–d** Compositional comparison (λ_1 versus λ_2, Sr versus Y, Nb versus Ta) between modeling melts derived from 9 kbar cases with varying bulk H_2O contents and TTGs. **f–h** Same compositional comparisons for the 15 kbar cases. Different bulk H_2O contents are represented by colors, with the numbers around the nodes indicating the degree of partial melting. The calculated melt fractions are from 5 to 50% at 5% intervals. The rise in pressure from 9 kbar to 15 kbar substantially enhances garnet proportions in the solid residue, prompting a compositional shift in the modeling melts from the "LP"-TTG region to the "HP"-TTG region.
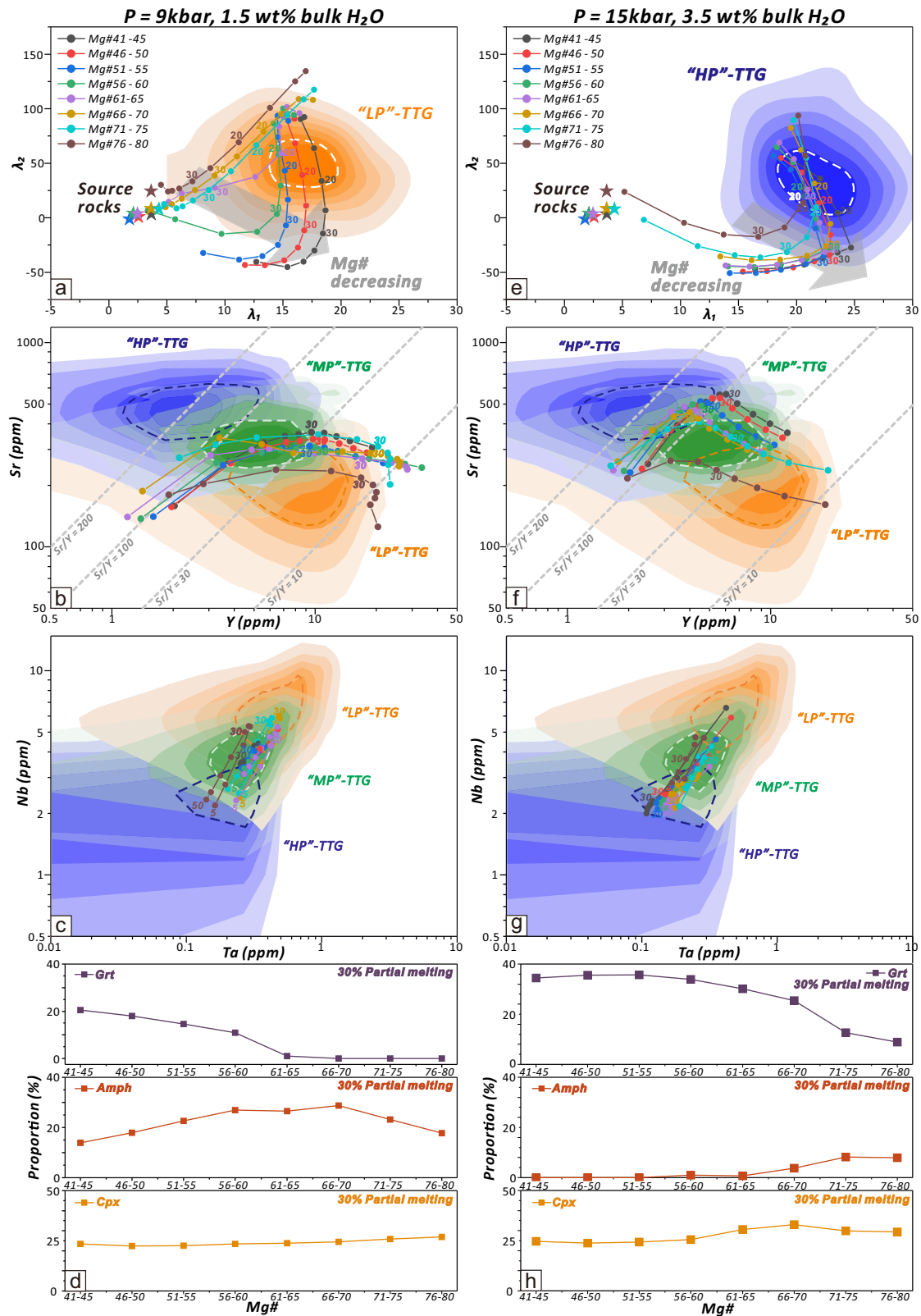
Fig. 6 | Geochemical modeling and calculated phase proportions for cases with varied source rock composition. The left column represents the calculated results of partial melting at the "LP"-TTG forming condition, while the right column stands for the results of partial melting at the "HP"-TTG forming condition. The P-X_{H2O} conditions for the formation of two types of TTGs are based on the thermodynamic modeling of median enriched Archean basalt[27]. **a–c, e–g** Compositional comparison (λ_1 versus λ_2, Sr versus Y, Nb versus Ta) between modeling melts derived from source rocks with varying Mg# and TTGs. Different colors stand for different Mg# of source rock, and the numbers around the nodes indicate the degree of partial melting. The calculated melt fractions are from 5 to 50% at 5% intervals. **d, h** Calculated modal proportion of minerals (garnet, amphibole, and clinopyroxene) versus Mg# of source rock, with the partial melting degree fixed at 30%. See Supplementary Fig. 15 for similar modeling based on "MP"-TTG forming condition.
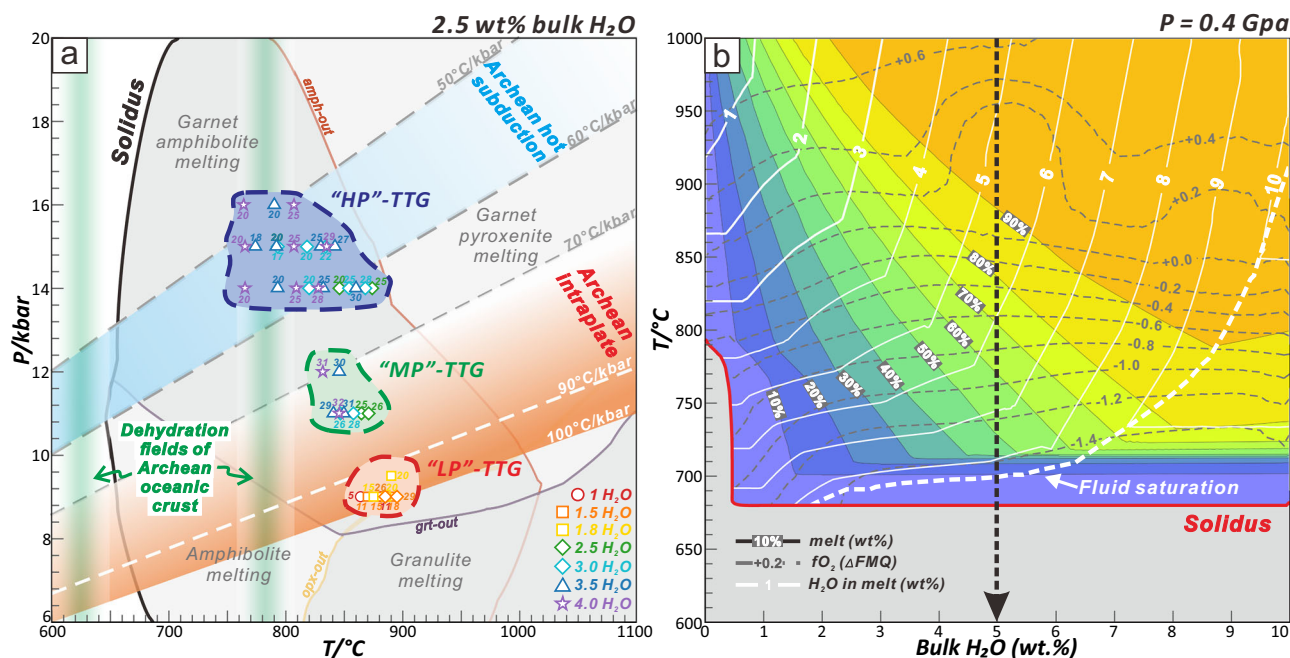
Fig. 7 | Thermodynamic modeling results. a Simplified P-T phase diagram for median enriched Archean basalt[27], calculated with 2.5 wt.% bulk H_2O. The optimal P-T regions for "LP"-, "MP"-, and "HP"-TTG forming are outlined by red, green, and blue dashed lines, respectively. The apparent geothermal gradients of "HP"-TTGs forming conditions are consistent with those proposed for Archean hot subduction[72,116], while the apparent geothermal gradients for "LP"- and "MP"-TTGs forming in line with Archean intraplate geothermal gradients[55,56]. The optimal X_{H2O} conditions for the formation of these three types of TTGs are shown by hollow shapes with edges of different colors. Two green columns represent the two main temperature ranges for dehydration of Archean oceanic crust[58,63]. **b** Simplified T-X_{H2O} phase diagram for median sodic TTG magma[8], with pressure fixed at 4 kbar. The contours showing modal proportions of melt fraction (colored field and grey lines) and H_2O content in the melt (white lines) are calculated in our modeling. The isopleth diagram for magmatic fO_2 (grey dashed lines) is from ref. 29. The bolded dashed lines with arrows represent the crystallization of TTG magma at 4 kbar, with the initial H_2O contents of 5 wt.%. During this process, the rising of magmatic H_2O content is accompanied by the decline of magmatic fO_2, which is driven by the crystallization of ilmenite and amphibole[29]. More importantly, declining from 1000 °C to 800 °C (predicted saturation temperature for zircon[33]), H_2O content in melt increases by only ~1 wt.%.

Archean TTGs at ~700–900 °C, 9–16 kbar, and 1–4 wt.% bulk H_2O, corresponding to ~15–30% partial melting (Fig. 7a and Supplementary Figs. 10–14). Specifically, "LP"-TTGs may form at 9–9.5 kbar, 1–1.8 wt.% H_2O through fluid-absent melting, whereas the formation of "HP"-TTGs plausibly requires high-pressure fluid-fluxed melting (14–16 kbar, 2.5–4.0 wt.% H_2O). "MP"-TTGs can form at intermediate conditions. Based on these results, we suggest that the primary melts of different TTG types may have distinct H_2O contents, i.e., higher for "HP"-TTGs than "LP"-TTGs.

To verify the above modeling results, we applied an apatite-based melt hygrometric calculation approach to TTGs (**Methods**). This hygrometer is established by integrating an existing thermodynamic model for F–Cl–OH partitioning between apatite and silicate melts[31], with known relations between melt halogen contents and their mole fraction ratios[45]. A test using natural volcanic suites with well-known H_2O contents shows that the magmatic H_2O contents calculated by the apatite hygrometer agree well with those measured for melt inclusions, with differences of less than 1.5 wt.% on average (Fig. 8b). Notably, only apatite fully enclosed by oscillatory-zoned zircon is considered in this study, to minimize the interference from diffusive re-equilibration of volatiles in apatite[46] and overprint during high-grade metamorphism[47] (Supplementary Fig. 3). The results calculated from apatite show that "HP"-TTGs have the highest melt H_2O contents (~8.0 wt.%), whereas the "LP"-TTGs have the lowest (~4.5 wt.%), matching our prediction of the optimal H_2O contents for TTG melts (Fig. 8c).

The melt H_2O content recorded by apatite is governed by: (1) primary melt H_2O content; (2) fractional crystallization; and (3) magma degassing. During the emplacement and cooling of TTG melts, the H_2O content can increase with fractionation (before saturation) but will show a negative correlation with oxygen fugacity (fO_2) (Fig. 7b). This trend contradicts the observation of a positive correlation between calculated melt H_2O contents

and measured apatite SO_3 contents (Fig. 8a, c), as sulfur incorporation in apatite is strongly fO_2-dependent[48]. The agreement with fO_2 estimates[49] further rules out the influence of crystallization. Additionally, TTG magmas are typically emplaced at mid-crustal depths (3–7 kbar)[12,50], where the H_2O solubility (>8 wt.%)[51] is significantly higher than the melt H_2O contents we calculated from apatite. This indicates a negligible effect of degassing-induced H_2O depletion. Collectively, these observations support the conclusion that the H_2O contents calculated from our apatite dataset likely represent those of primary magmas.

Importantly, similar trends in magmatic H_2O contents across different TTG types are also observed in the melt H_2O contents estimated from a zircon hygrometer[29]. These values are slightly higher than those derived from apatite inclusions by 1–2 wt.% (Fig. 8c), probably due to magma evolution between the crystallization of apatite and zircon. This is also supported by our thermodynamic models showing that the H_2O content of TTG magma varies by ~1 wt.% when the magma cools from 900 to 800 °C (Fig. 7b). The comparable H_2O contents recorded by the two minerals indicate crystallization at pressures where the melt H_2O content is buffered[52] and represent that of the primary magma. Given the limited number of apatite samples suitable for analysis (Fig. 8c), the global-scale zircon dataset from Ge et al.[29] may provide a more universal perspective on magmatic H_2O contents of Archean TTGs. Although their dataset indicates variations in magmatic H_2O contents with zircon U-Pb ages, large differences were indeed observed between TTG types, with "HP"-TTGs ranging from 8 to 11 wt.% and "LP"-TTGs ranging from 4 to 6 wt.% (Fig. 8d). These values are consistent with those obtained from our apatite dataset, and more importantly, are in close accordance with the H_2O contents predicted for the optimal TTG melts from this study (Fig. 8d). Furthermore, Ge et al[29]. pointed out strong correlations between magmatic fO_2-H_2O content and whole-rock compositions, with the high-fO_2, H_2O-rich "HP"-TTGs
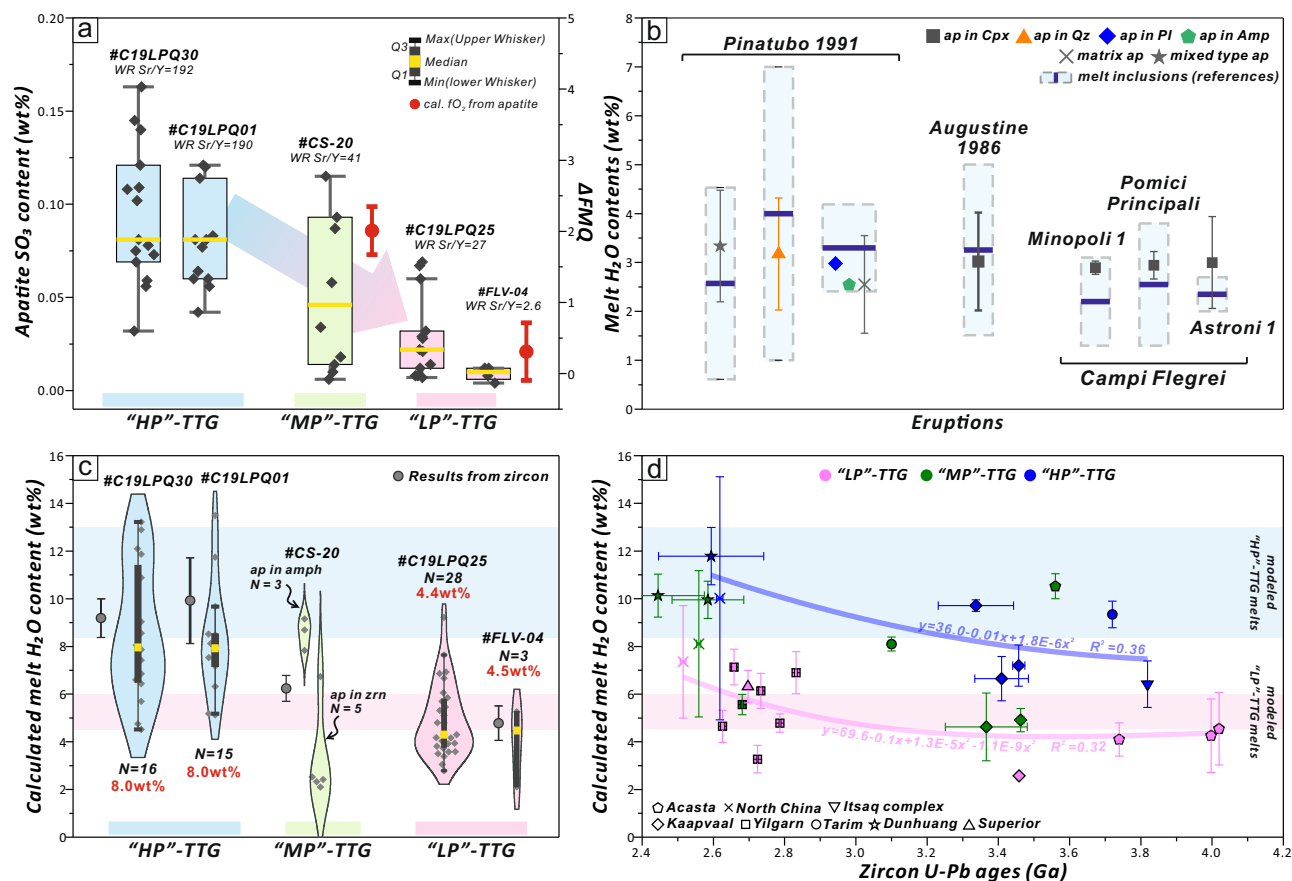
Fig. 8 | Calculated results from apatite and zircon. a Box plot of SO_3 contents of compiled Archean TTG apatite (Supplementary Table 7). The calculated $fO2$ values (relative to the fayalite-magnetite-quartz buffer) for sample CS-20 and FLV-04 are also shown, which are estimated based on the ratios of S^{6+} to total sulfur in apatite[49]. **b** Comparison of the magmatic H_2O content estimated using the apatite hygrometer (this study) and melt inclusions (the literature) for five eruptions. The light blue-filled rectangles represent the reference values of magmatic H_2O content measured from melt inclusions, with the dark blue line indicating the mean value (Supplementary Table 6). The magmatic H_2O contents from different types of apatite grains totally overlap with those from melt inclusions, with the differences in mean values being less than 1.5 wt.%. **c** Violin plots of magmatic H_2O contents (wt.%) calculated using the TTG apatite dataset in this study (Supplementary Table 7). The intra-sample calculated H_2O contents show a range of variation, especially for sample CS-20. Given the similarity in apatite volatile compositions within the same sample

(Supplementary Fig. 4), we suggest that the discrepancies may stem from deviations between the crystallization temperature of a single apatite grain and the apatite saturation temperature (AST) used for calculation. After excluding outliers, the median value is used to represent the magmatic H_2O content recorded by apatite for each sample (**Methods**). The yellow stripes represent the median values. The calculated melt H_2O contents based on zircon in the same sample are also shown (Supplementary Table 8). Notably, the insufficient number ($N = 3$) of zircon data from sample C19LPQ25 suitable for the zircon hygrometer[29] makes it difficult to accurately calculate the melt H_2O content. **d** Magmatic H_2O contents estimated from the global Archean TTG zircon dataset, which was mainly compiled by ref. 29. and supplemented by new data from the North China Craton (Supplementary Table 8). The magmatic H_2O content ranges of optimal modeled melts for "LP"- (pink band), and "HP"-TTGs (blue band) are also shown, which overlap with the H_2O contents estimated from zircon and apatite.

exhibiting larger extents of garnet and rutile differentiation, consistent with our model results. As a whole, the above-mentioned mineralogical evidence validates the optimal melting conditions we found for Archean TTGs formation.

Geodynamic implications for the early Earth

The Archean mantle is thought to have been significantly hotter than today[53]. Under such hot circumstances, intensified partial melting of mantle accompanied by enhanced mantle convection could have led to an Archean oceanic crust that was much thicker than present and may be ~30 km (up to 45 km) in thickness[43,53,54]. Moreover, the elevated conductive heat from the hot Archean mantle, in conjunction with high radioactive heat production within the upper Archean crust, raised the vertical geothermal gradient of the intraplate regions in the early Earth to be >70 °C/kbar, up to ~95 °C/kbar (refs. 9,55–57) (Fig. 7a).

By integrating thermodynamic modeling with constraints from apatite and zircon, we proposed that "LP"- and "MP"-TTGs likely formed at similar temperatures but different pressures, yielding apparent geothermal gradients of 90–100 °C/kbar and 70–80 °C/kbar, respectively

(Fig. 7a). These P-T conditions are congruent with the lower-crustal thermal structure of the intraplate regimes described above, indicating a potential derivation of these two types of TTGs from the anatexis of lower Archean mafic crust. Furthermore, intraplate environments with a geothermal gradient exceeding 90 °C/kbar ("LP"-TTGs forming conditions) would significantly limit the ability of hydrated mafic-ultramafic crustal materials to transport large amounts of H_2O from near surface to lower crustal depths through burial or dripping, as key hydrous minerals (e.g., chlorite) could dehydrate at pressures below 6–7 kbar (ref. 58) (Fig. 7a). The mantle-derived magma unrelated to subduction is typically dry (of <0.5 wt.% H_2O; refs. 30,52,59) and unlikely to supply abundant H_2O (ref. 60). These lines of evidence suggest that in the Archean hot intraplate setting, the lower crust may be mainly subject to fluid-absent melting, in agreement with the optimal melting conditions we found for "LP"-TTGs. The intracrustal fluid-fluxed melting required for "MP"-TTGs formation likely occurred under cooler conditions (with ~70 °C/kbar), where near-surface hydrated komatiites, which may result from mantle plume or heat-pipe activities[61,62], could stabilize hydrous minerals at higher pressures (~11 kbar; refs. 58,63) (Fig. 7a).
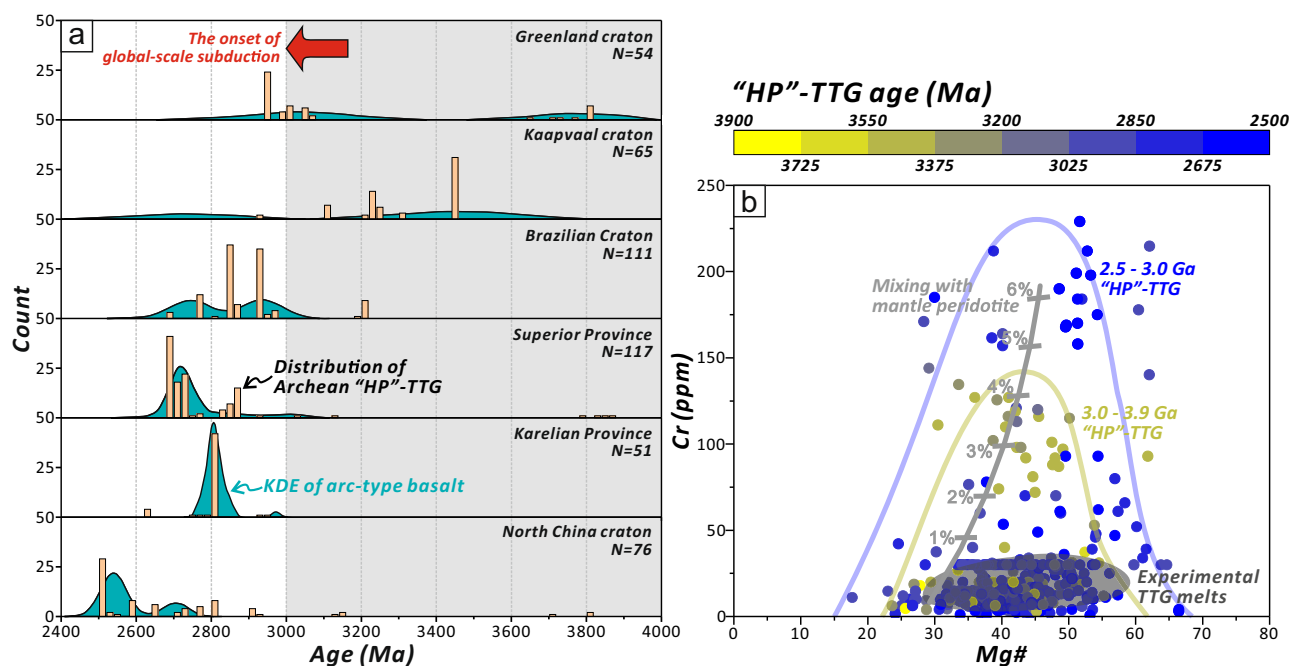
Fig. 9 | Temporal distribution and evolution of TTGs. a Histogram of the ages of Archean "HP"-TTGs (light-orange) from different cratons. The numbers in the right corners represent the number of "HP"-TTG data. Kernel density estimations of the Archean arc-type basalts predicted through machine learning (cyan) are from ref. 70. The appearance of "HP"-TTGs aligns closely with that of arc-type basalts. **b** Cr versus Mg#. The "HP"-TTGs with the ages of 3.0–3.9 Ga have higher Cr content than experimental TTG melts[72] but lower Cr content than "HP"-TTGs with ages of 2.5–3.0 Ga, showing limited interaction with the mantle wedge. The vector of mixing with mantle peridotite comes from ref. 27.

However, it is substantially challenging for the intraplate tectonic setting outlined above to achieve the deep (14–16 kbar) and H_2O-enriched (2.5–4 wt.%) conditions needed for "HP"-TTGs formation (Fig. 7a). Owing to the hot mantle and abundant radioactive isotopes, the Archean crust has a great tendency to trigger both lower- and upper-crustal ductile flows, accordingly impeding the steady occurrence of thickened mafic crust induced by mantle plume system and restricting the crustal thickness to be ≤45 km (refs. 64,65). This suggests that the formation of "HP"-TTGs probably occurs at subcrustal depths. However, density-driven vertical movement is unlikely to force the mafic crustal materials ("drips") to penetrate the lower crust into the mantle, as the latter has similar or even higher densities. Even if these "drips" manage to reach the melting depth, prograde dehydration induced by the high geothermal gradient of intraplate settings could cause the loss of a majority of H_2O (refs. 58,66).

Alternatively, subduction of hydrated oceanic slabs offers an efficient way to transport fluids and mafic materials to a deeper level[67]. Numerical modeling suggests that hot and shallow (~50 km depth) subduction could occur in the early Earth when the mantle potential temperature difference relative to the present-day value (ΔT_p) was ≤200 °C (refs. 68,69). Along the geothermal gradients proposed for subducting Archean slabs, which align closely with those we found for "HP"-TTGs formation, dehydration of hydrated Archean oceanic crust was predicted to occur at different pressures (Fig. 7a): (1) At ~11 kbar, corresponding to the base of the overlying crust, the breakdown of antigorite/actinolite will release a small amount of H_2O (~20% mol; refs. 23,58,63), which may directly migrate to the overlying slab. As the geothermal gradients inferred for the overlying Archean slabs (~80 °C/kbar)[69] coincide with those we found for "MP"-TTGs formation, the early-stage dehydration of subducting Archean slabs will facilitate "MP"-TTG generation. (2) At ~15 kbar, corresponding to the melting depth for "HP"-TTGs, a large proportion of H_2O (~60% mol) will be released due to chlorite breakdown[23,58,63], thereby triggering fluid-fluxed melting of slab or mantle wedge metasomatism. The critical role that subduction plays in the formation of "HP"-TTGs was also suggested by the global-scale

temporal synchronicity between the emergence of arc-type basalts (predicted by machine learning methods[70]) and "HP"-TTGs (Fig. 9a), as well as the similarity in magmatic H_2O contents between "HP"-TTGs and Phanerozoic arc magmas[29]. More importantly, Archean "HP"-TTGs, though of lower Mg#, nickel (Ni), and chromium (Cr) contents than modern adakites, show markedly higher contents of these elements than the melts resembling "HP"-TTG produced by experimental basalt melting (Fig. 9b). This emphasizes that interaction with the mantle wedge is an essential process in the formation of "HP"-TTG, but the degree of mixing with mantle peridotite is limited (≤3%), probably suggesting the occurrence of shallow subduction in the hot early Earth, with a small thickness of the overlying mantle wedge[17,71,72]. In light of these findings, we inferred that Archean "HP"-TTGs likely originated from the melting of the subducting slabs. Moreover, the underplating of felsic and mafic melts may have triggered fluid-absent melting of the overlying crust to form "LP"-TTGs[19], allowing different types of TTGs to appear simultaneously in the same area[8].

Drawing from these tectonic implications of different types of Archean TTGs, we can explore the geodynamic background of the early Earth and the timing of the transition in tectonic regimes, which are profoundly governed by the lithospheric thermal state[3,73]. During the earliest stages of the Earth's evolution (≥3.8 Ga), subduction was unfeasible to happen under the extremely hot mantle (ΔT_p ≥ 250 °C), owing to the significant weakening of lithosphere[68,69,74], giving way to extensive intracrustal anatexis within the stagnant-lid background[20]. This probably accounts for the prevalence of "LP"- and "MP"-TTGs in early Eoarchean granitoids (Supplementary Fig. 8). Along with the progressive cooling of the mantle[75] and the decline of radiogenic heat production[56], gradually elevated rigidity of lithosphere could facilitate the initiation of episodic and shallow subduction of smaller and thicker oceanic slabs[17,76,77], driving the emergence of "HP"-TTGs and arc basalts, as well as "MP"-TTGs. Notably, the formation of "MP"-TTGs in both geodynamic settings may have played a key role in their predominance throughout the Archean[8]. However, subduction seems to arise from localized cooling heterogeneity[78], as evidenced by the temporal

differences in the earliest appearance of "HP"-TTGs across different regions (Fig. 9a). Only when the optimal conditions for subducting (e.g., mantle temperature, radiogenic heat production, lithospheric thickness; refs. 69,79) are satisfied in most regions will global-scale subduction (plate tectonic) be activated, leaving widespread geological records. Based on the abrupt increase in magmatic H_2O contents and the fO_2 of global Archean TTGs, Ge et al.[29] proposed that the tectonic regime transition from stagnant-lid to plate tectonics may have occurred between 4 and 3.6 Ga. However, this period may only represent the initiation of the first localized subduction in early Earth (e.g., 3.8 Ga in Greenland; Figs. 8d and 9a), which leads to the emergence of high-H_2O, high-fO_2 "HP"-TTGs, but may not stand for the onset of global plate tectonics. Considering the global occurrence of "HP"-TTGs and arc-type basalts, we speculated that the onset of global subduction may have been delayed until ~3.0 Ga (Fig. 9a). By this time, mantle potential temperature had likely decreased to <1500 °C (ref. 75), a threshold under which numerical modeling predicts that hot subduction could operate[69]. Independent lines of evidence from global geochemical[78,80,81], petrological[82,83], and geodynamic[84,85] studies also support the timing of ~3.0 Ga.

Methods

Thermodynamic and geochemical modelling

Thermodynamic modeling was carried out with the software *GeoPS*[41], using the thermodynamic database HP62[86] and solution models for tonalitic melt, amphibole and clinopyroxene from ref. 87, orthopyroxene, garnet, muscovite, chlorite and biotite from ref. 88, plagioclase and K-feldspar from ref. 89, ilmenite from ref. 90, magnetite-spinel from ref. 91, olivine and epidote from ref. 86. Pure phases included quartz, rutile, sphene, and aqueous fluid (H_2O). To compare the effect of pressure and water content on melt composition, we conducted 15 sets of isobaric melting modeling, with pressures of 8 to 10 kbar. Each set includes seven models of different bulk H_2O contents, ranging from 1 to 4 wt.% (Supplementary Table 1). The source rock and temperature range for these 105 modeling was set to be median enriched Archean basalt from ref. 27. (Supplementary Table 2) and 600–1200 °C. Bulk rock $Fe^{3+}/\sum Fe$ ratios were set to be 0.1, which is typical of mafic lavas on the early Earth[36]. To determine the effect of source rock composition (Mg#), the global Archean basalts compiled by ref. 92. ($N = 2304$) were categorized into eight groups based on their Mg# values, i.e., from 41 to 80, with each group spanning Mg# of 5. Three more sets of melting modeling were conducted, with melting conditions (P-X_{H2O}) of each set corresponding to the optimal ones for "LP"- (9 kbar, 1.5 wt.% H_2O), "MP"- (11 kbar, 3.0 wt.% H_2O), and "HP"-TTGs (15 kbar, 3.5 wt.% H_2O) forming, respectively. These conditions were constrained by the compositional comparison of modeled melts from the prior 105 runs with global Archean TTGs. Each set included eight modeling, with their source rocks corresponding to the average bulk composition of each Archean basalt group (Supplementary Table 2). The summary of thermodynamic modeling parameters for these 129 runs can be found in Supplementary Table 1.

Mode (wt.%) and major element compositions (including H_2O contents) of melts and equilibrium mineral assemblages were obtained from the software *GeoPS* (Supplementary Table 4). Trace element compositions of modeling melts were calculated through the batch melting equation:

$$C_{melt}/C_{source} = 1/[D + F \times (1 - D)] \qquad (1)$$

where C_{melt} and C_{source} represent concentrations of a trace element in the resultant melt and the source rock, respectively; F is the melt fraction (wt.%); D is the bulk partition coefficient calculated using mineral mode and corresponding partitioning coefficient. The zircon and apatite proportions present in the melt-depleted residua are calculated through source rock composition, melt fraction, and stoichiometric concentrations of zirconium (Zr) in zircon (~49.7 wt.%) and phosphorus (P) in apatite (~41.0 wt.%). Solubility expressions for zircon and apatite were from ref. 93 and ref. 94, respectively. Partition coefficients (Supplementary Table 3) were mostly cited from ref. 95, except for those for amphibole[24], Nb and Ta data for rutile

and ilmenite[96], and Sr data for plagioclase[14]. The calculated melt compositions (Supplementary Table 4) were compared with those of Archean "LP"-, "MP"- and "HP"-TTGs in terms of major elements, λ shape coefficients, and Sr/Y, Nb/Ta ratios (Supplementary Figs. 10–14). The λ shape coefficients were first introduced by O'Neill et al.[38] to quantify the polynomial characterization of CI-normalized REE pattern shapes. The polynomial can be presented in orthogonal form:

$$log_{10}([REE]/[REE]_{CI}) = \lambda_0 + \lambda_1 F_1 + \lambda_2 F_2 + \ldots + \lambda_n F_n \qquad (2)$$

where [REE] and $[REE]_{CI}$ are the abundance of each REE in sample and chondrite, respectively, F_n is the orthogonal polynomial function of commonly used ionic radii of each REE (eightfold coordination), and λ_n is the shape coefficient of the whole set of REE. As the order of function rises (increase in n), the morphological characteristic of REE curve expressed by λ_n varies, i.e., λ_0 for the overall normalized abundance of the REE, λ_1 for the linear slope, and λ_2 for the quadratic curvature. Using λ coefficients to represent REE patterns can diminish the dimension of each analysis from a line to a point. In this study, the λ shape coefficients of TTGs and modeling melts are calculated through *BLambdaR*, an online calculator (https://lambdar.rses.anu.edu.au/blambdar/)[97].

Data compilation and filtering

The global-scale Archean TTG dataset used in this study was adopted from ref. 98, which excludes altered TTG samples. Besides, we supplemented Eoarchean TTG data from Tarim Craton[27,99]. While no strict quantitative compositional definition of TTG exists, following the criteria of Johnson et al.[100], we exclude more evolved granitic rocks (sensu stricto), sanukitoids, and felsic cumulate rocks by restricting our dataset to samples with (1) $SiO_2 \geq 65$ wt.%; (2) $K_2O/Na_2O \leq 0.8$. Additionally, to improve the accuracy of calculated λ coefficients of TTGs, whole-rock data with less than seven available REE contents were discarded, as low counts increase uncertainty, shown by scattered points in the λ_1 versus λ_2 plot[97]. The final dataset for global Archean TTGs contains 1960 samples (Supplementary Table 5), which are distributed within the global craton (Supplementary Fig. 19).

To accurately classify TTGs, we adopted the classification scheme of ref. 8, which is based on whole-rock major and trace element characteristics and integrates both manual and automated groupings through naive Bayes classification. Although this scheme originally separates TTGs into "LP"-, "MP"-, and "HP"-TTGs using a wide range of elemental concentrations and ratios, Sr/Y, Ce/Sr, and Eu/Gd ratios are demonstrated to be the most effective discriminants. Accordingly, we classify the global Archean TTGs into "LP"- ($N = 476$), "MP"- ($N = 848$), and "HP"-types ($N = 636$) using the Sr/Y, Ce/Sr, and Eu/Gd ranges defined by ref. 8. Importantly, not all of these proxies are sensitive to pressure or magmatic H_2O content, ensuring that our modeling results on the controlling factors of Archean TTG compositions are robust. In comparison with modeling melts to determine the optimal melting conditions for different types of TTGs, the reference compositional range for each TTG type was defined as the intervals with data density ≥70%, based on kernel density estimations (Fig. 1). Notably, although the quantity of TTG samples is not evenly distributed for different ages (Supplementary Fig. 8), the integration of data can be considered as a random collection of publications without an arbitrary bias for a certain age. More importantly, from the Paleoarchean to the Neoarchean, "LP"-, "MP"-, and "HP"-TTGs are not restricted to, nor dominated by, any single craton, but instead derive from a global assemblage of samples (Supplementary Fig. 8). This suggests that our dataset is unlikely to be significantly affected by preservation or sampling biases, and can be regarded as broadly representative of global TTG magmatism during this interval. In contrast, the Eoarchean record is more limited, particularly for "HP"-TTGs ($N = 29$), most of which are restricted to the Greenland craton ($N = 11$). Other Eoarchean TTG types, however, display diverse cratonic origins with relatively even distributions. For example, Eoarchean "MP"-TTGs in our dataset are from the Greenland craton ($N = 15$), Slave craton ($N = 13$), North China craton ($N = 9$), and Superior Province ($N = 5$). Given that TTG

classification relies primarily on trace element characteristics rather than field occurrences, we argue that the Eoarchean "HP"-TTG dataset is unlikely to be significantly biased by uneven sampling. Furthermore, in light of machine learning results on Archean basalts, which predict that subduction in the Eoarchean may have been confined to the Greenland craton[70], together with field observations and geochemical analyses that also indicate early intra-oceanic subduction processes within this craton around 3.8–3.7 Ga[101–103], we infer that the limited distribution of Eoarchean "HP"-TTGs likely records localized subduction in early Earth rather than preservation bias.

Apatite data for TTGs were compiled based on the following criteria: (1) apatite must be fully enclosed within oscillatory-zoned zircon to ensure its magmatic origin, and (2) apatite volatile compositions do not exhibit evidence of H_2O saturation (e.g., extremely low X_{Cl}/X_{OH} ratio and extremely high X_F/X_{Cl} ratio in apatite[104]), since the calculation of magmatic H_2O content relies on the volatile-undersaturated case (see below). However, studies on apatite inclusions hosted by zircon within TTGs remain scarce. Apatite inclusion data from refs. 105–108. are discarded due to the alteration or crystallization at H_2O-saturated conditions (Supplementary Fig. 4). Only apatite inclusions from sample CS-20 and FLV-04 (ref. 109) pass the screening. To enhance the sample size in our analysis, we obtained new data for apatite and zircon from the Aktash gneisses complex, Tarim Craton (samples C19LPQ01, C19LPQ25, C19LPQ30). These three grey gneisses are enriched in Na_2O, with the Na_2O/K_2O ratios of 2.2–5.1, and exhibit intense fractionation of REE (chondrite-normalized La/Yb ratios up to 100), showing the characteristics of TTGs (Supplementary Fig. 5). Only apatite inclusions fully enclosed by oscillatory-zoned zircon are analyzed (Supplementary Fig. 3). Detailed information on the geological background and analytical methods can be found in Supplementary Notes 1 and 2. The combined data for apatite ($N = 77$; Supplementary Table 7) cover all three major TTG types, with samples C19LPQ01 and C19LPQ30 being classified as "HP"-TTGs, CS-20 as "MP"-TTG, and C19LPQ25 as "LP"-TTG.

The global Archean TTG zircon dataset is mainly compiled by ref. 29 and is supplemented by new data from the North China Craton[110]. The combined data for zircon ($N = 1012$) is shown in Supplementary Table 8. Following the method of ref. 29, we estimated the magmatic H_2O contents of Archean TTGs from the zircon dataset.

Calculating magmatic H_2O contents by apatite

The partitioning of volatile (F–Cl–OH) between apatite and silicate melts has been found to show non-Nernstian behavior[111,112], i.e., the estimate of magma H_2O content cannot be simply obtained from the apatite-melt H_2O partition coefficients. Instead, the partitioning behavior was found to be better expressed by the exchange coefficients (K_D) for two components among F, Cl, and OH:

$$K_{D_{OH-Cl}}^{Ap-melt} = (X_{OH}^{Ap} \cdot X_{Cl}^{melt})/(X_{Cl}^{Ap} \cdot X_{OH}^{melt}) \tag{3}$$

$$K_{D_{OH-F}}^{Ap-melt} = (X_{OH}^{Ap} \cdot X_{F}^{melt})/(X_{F}^{Ap} \cdot X_{OH}^{melt}) \tag{4}$$

where X is the mole fraction of volatile in apatite or in the melt. Li and Costa[31] carried out a weighted least squares regression on the K_D determined by multiple experiments, proposed multivariate linear equations (using apatite F–Cl–OH composition and temperature as variables) for expressing $K_{D_{OH-Cl}}^{Ap-melt}$ and $K_{D_{OH-F}}^{Ap-melt}$ (see Eqs. 5 and 6 below), and established a robust calculation procedure for estimating the H_2O contents in melt by apatite volatile contents. We adopt this method and conduct the calculation using a Python module $pyAp$ (https://doi.org/10.5281/zenodo.6228767).

$$lnK_{D_{OH-Cl}}^{Ap-melt} = -1/(RT) \times [72900(\pm 2900) - 34(\pm 0.3) \times T + 1000$$
$$\times \left(5(\pm 2) \times \left(X_{Cl}^{Ap} - X_{OH}^{Ap}\right) - 10(\pm 8) \times X_F^{Ap}\right)] \tag{5}$$

$$lnK_{D_{OH-F}}^{Ap-melt} = -1/(RT) \times [94600(\pm 5600) - 40(\pm 0.1) \times T + 1000$$
$$\times \left(7(\pm 4) \times \left(X_F^{Ap} - X_{OH}^{Ap}\right) - 11(\pm 7) \times X_{Cl}^{Ap}\right)] \tag{6}$$

A prerequisite for calculating magma H_2O content (X_{OH}^{melt}) using these equations is a known F (X_F^{melt}) or Cl (X_{Cl}^{melt}) content of the melt in equilibrium with apatite (Eqs. 3 and 4). For some igneous samples, these can be determined by analysing melt inclusions within the same samples and/or calculations using fractionation models (e.g., ref. 113). However, melt inclusions are rare and greatly altered in Archean TTGs. Kendall–Langley et al.[45] reported a strong correlation ($R^2 > 0.95$) between the concentrations of F (or Cl) and X_F^{melt}/X_{OH}^{melt} (or $X_{Cl}^{melt}/X_{OH}^{melt}$) in the melt through compiling data from partitioning experiments, and accordingly deduced the equations for estimating the melt F, Cl contents solely using F–Cl–OH composition of apatite (see Eqs. 7 and 8 below). With the melt Cl or F contents calculated from these equations, we calculated two magmatic H_2O contents using the two exchange coefficient equations (i.e., Eqs. 5–6).

$$C_{Cl}^{melt} = K_{D_{OH-Cl}}^{Ap-melt} \times (X_{Cl}^{Ap}/X_{OH}^{Ap}) \times 8.7058 \, (R^2 = 0.9578) \tag{7}$$

$$C_F^{melt} = K_{D_{OH-F}}^{Ap-melt} \times (X_F^{Ap}/X_{OH}^{Ap}) \times 4.6978 \, (R^2 = 0.9528) \tag{8}$$

It is important to point out that the above equations describing the behavior of F–Cl–OH partitioning between apatite and melt are predicted on experimental systems in which the volatile is undersaturated. Hence, the applications of them are limited to volatile-undersaturated magmas. By comparing the apatite volatile compositions with modeling results from ref. 104, magmatic H_2O can be determined to be saturated or not, but the halogens (F, Cl) are unknown. In silicate magmas, the saturation and subsequent exsolution of halogens from a magmatic liquid are sensitive to the magma composition[51,114]. The solubility of F will increase up to a factor of 6–7 as the melt evolves (with a decrease in NBO/T), whereas the Cl solubility shows the opposite, with a decline as NBO/T descends. Thus, in the process of magmatic evolution within the magma chamber, F exhibits more stable characteristics than Cl and is less susceptible to saturation and exsolution. Moreover, F does not form a separate brine, as does chlorine, at concentrations similar to those found in magmatic systems[115]. For these reasons, we consider that the probability of Cl within the melt being disrupted by saturation at the time of apatite crystallization is much greater than that of F. Hence, we calculated the magmatic H_2O content based on melt F content. The uncertainty of calculated melt H_2O content through the method in this study principally derives from: (1) analytical relative errors in apatite and whole-rock compositions, which are typically ≤5% for major elements; (2) calibration uncertainties in the formulation for $K_{D_{OH-F}}^{Ap-melt}$ (≤40–50% relative error). The propagated relative uncertainty in melt H_2O content is estimated to be ≤50%.

The accuracy of this method was assessed by recalculating the H_2O contents for natural magmatic suites with well-constrained H_2O concentrations (Fig. 8b). The natural apatite and melt inclusions compiled in ref. 31 are re-assessed, including those from the Mt. Pinatubo 1991 eruption, the Augustine 1986 eruption, and the Campi Flegrei (Minopoli 1, Astroni 1, Pomici Principali). These magmatic systems span a wide range of temperatures and melt compositions (Supplementary Table 6). Notably, these melt inclusions are in a similar textural position as apatite, demonstrating that their H_2O contents may represent those of the melts in equilibrium with apatite. The magmatic H_2O contents from different types of apatite grains overlap with those from melt inclusions, with the differences in mean values being less than 1.5 wt.%. These indicate that the approach we used to calculate magma H_2O content is reliable.

The experimental data considered in the method we used span from basic to felsic magma at 0.5 to 25 kbar, covering the crystallization

conditions of TTG magmas of interest (3–7 kbar, intermediate to felsic). Using the TTG apatite dataset (Supplementary Table 7), we calculate the H_2O contents of TTG magmas at temperatures equivalent to the estimated apatite saturation temperatures (AST)[94]. This could be higher than the true apatite-melt equilibrium temperature and may produce underestimated melt H_2O content. For example, a temperature variation of 10 °C can result in a deviation of ~1.5 wt.% in the calculated melt H_2O content. This effect is mainly observed in sample CS-20 (Fig. 8c), where apatite inclusions in different textural positions (e.g., as inclusions in amphibole and zircon) yield a considerable variation in the calculated magmatic H_2O contents. These variations can be caused by different crystallization temperatures of apatite within different minerals, and/or different melt F–Cl contents at which the apatite grew. Given the similarity in volatile compositions among apatite inclusions hosted by zircon and amphibole from sample CS-20 (Supplementary Fig. 4), which indicates that these apatite grains probably crystallized in conditions with similar magmatic volatile states, we consider that the dispersed calculated magmatic H_2O contents are probably caused by the differences between the AST and the true apatite-melt equilibrium temperature. To make a comparison between samples, we take the median of the melt H_2O estimates from each sample. The outliers, which are data points falling outside the range of upper and lower whiskers, are not considered in the determination of the median values (Fig. 8c).

Data availability
All data used in this study (Supplementary Table 1 to Table 9) are archived on Zenodo (https://doi.org/10.5281/zenodo.17376497).

References
1. Martin, H., Smithies, R., Rapp, R., Moyen, J.-F. & Champion, D. An overview of adakite, tonalite–trondhjemite–granodiorite (TTG), and sanukitoid: relationships and some implications for crustal evolution. *Lithos* **79**, 1–24 (2005).
2. Moyen, J.-F. & Martin, H. Forty years of TTG research. *Lithos* **148**, 312–336 (2012).
3. Brown, M., Johnson, T. & Gardiner, N. J. Plate tectonics and the Archean Earth. *Annu. Rev. Earth Planet. Sci.* **48**, 291–320 (2020).
4. Laurent, O., Guitreau, M., Bruand, E. & Moyen, J.-F. At the dawn of continents: Archean tonalite-trondhjemite-granodiorite suites. *Elements* **20**, 174–179 (2024).
5. Rapp, R. P. & Watson, E. B. Dehydration melting of metabasalt at 8–32 kbar: implications for continental growth and crust-mantle recycling. *J. Petrol.* **36**, 891–931 (1995).
6. Palin, R. M., White, R. W. & Green, E. C. Partial melting of metabasic rocks and the generation of tonalitic–trondhjemitic–granodioritic (TTG) crust in the Archean: Constraints from phase equilibrium modelling. *Precambrian Res.* **287**, 73–90 (2016).
7. Zheng, Y.-F. Origin of continental crust on early Earth. *Natl. Sci. Rev.* **12**, nwaf341 (2025).
8. Moyen, J.-F. The composite Archaean grey gneisses: petrological significance, and evidence for a non-unique tectonic setting for Archaean crustal growth. *Lithos* **123**, 21–36 (2011).
9. Johnson, T. E., Brown, M., Gardiner, N. J., Kirkland, C. L. & Smithies, R. H. Earth's first stable continents did not form by subduction. *Nature* **543**, 239–242 (2017).
10. Liou, P. & Guo, J. Generation of Archaean TTG gneisses through amphibole-dominated fractionation. *J. Geophys. Res. Solid Earth* **124**, 3605–3619 (2019).
11. Laurent, O. et al. Earth's earliest granitoids are crystal-rich magma reservoirs tapped by silicic eruptions. *Nat. Geosci.* **13**, 163–169 (2020).
12. Kendrick, J., Duguet, M. & Yakymchuk, C. Diversification of Archean tonalite-trondhjemite-granodiorite suites in a mushy middle crust. *Geology* **50**, 76–80 (2022).
13. Hastie, A. R. et al. Deep formation of Earth's earliest continental crust consistent with subduction. *Nat. Geosci.* **16**, 816–821 (2023).
14. Qian, Q. & Hermann, J. Partial melting of lower crust at 10–15 kbar: constraints on adakite and TTG formation. *Contrib. Mineral. Petrol.* **165**, 1195–1224 (2013).
15. Rapp, R. P., Shimizu, N. & Norman, M. D. Growth of early continental crust by partial melting of eclogite. *Nature* **425**, 605–609 (2003).
16. Moyen, J. & Stevens, G. Experimental constraints on TTG petrogenesis: implications for Archean geodynamics. *Geophys. Monogr. Am. Geophys. Union* **164**, 149 (2006).
17. Moyen, J.-F. & Van Hunen, J. Short-term episodicity of Archaean plate tectonics. *Geology* **40**, 451–454 (2012).
18. Foley, S., Tiepolo, M. & Vannucci, R. Growth of early continental crust controlled by melting of amphibolite in subduction zones. *Nature* **417**, 837–840 (2002).
19. Ge, R., Wilde, S. A., Zhu, W., Zhou, T. & Si, Y. Formation and evolution of Archean continental crust: a thermodynamic–geochemical perspective of granitoids from the Tarim Craton, NW China. *Earth Sci. Rev.* **234**, 104219 (2022).
20. Bédard, J. H. Stagnant lids and mantle overturns: Implications for Archaean tectonics, magmagenesis, crustal growth, mantle evolution, and the start of plate tectonics. *Geosci. Front.* **9**, 19–49 (2018).
21. Capitanio, F., Nebel, O., Cawood, P., Weinberg, R. & Chowdhury, P. Reconciling thermal regimes and tectonics of the early Earth. *Geology* **47**, 923–927 (2019).
22. Furnes, H., Dilek, Y. D. & De Wit, M. Precambrian greenstone sequences represent different ophiolite types. *Gondwana Res.* **27**, 649–685 (2015).
23. Palin, R. M. & White, R. W. Emergence of blueschists on Earth linked to secular changes in oceanic crust composition. *Nat. Geosci.* **9**, 60–64 (2016).
24. Pourteau, A. et al. TTG generation by fluid-fluxed crustal melting: direct evidence from the Proterozoic Georgetown Inlier, NE Australia. *Earth Planet. Sci. Lett.* **550**, 116548 (2020).
25. Wang, X. et al. Adakite generation as a result of fluid-fluxed melting at normal lower crustal pressures. *Earth Planet. Sci. Lett.* **594**, 117744 (2022).
26. Laurie, A. & Stevens, G. Water-present eclogite melting to produce Earth's early felsic crust. *Chem. Geol.* **314**, 83–95 (2012).
27. Ge, R., Zhu, W., Wilde, S. A. & Wu, H. Remnants of Eoarchean continental crust derived from a subducted proto-arc. *Sci. Adv.* **4**, eaao3159 (2018).
28. Rollinson, H. Do all Archaean TTG rock compositions represent former melts?. *Precambrian Res.* **367**, 106448 (2021).
29. Ge, R.-F., Wilde, S. A., Zhu, W.-B. & Wang, X.-L. Earth's early continental crust formed from wet and oxidizing arc magmas. *Nature* **623**, 334–339 (2023).
30. Kelley, K. A. & Cottrell, E. Water and the oxidation state of subduction zone magmas. *Science* **325**, 605–607 (2009).
31. Li, W. & Costa, F. A thermodynamic model for F-Cl-OH partitioning between silicate melts and apatite including non-ideal mixing with application to constraining melt volatile budgets. *Geochim. Cosmochim. Acta* **269**, 203–222 (2020).
32. Huang, W. et al. Determining the impact of magma water contents on porphyry Cu fertility: constraints from hydrous and nominally anhydrous mineral analyses. *Bulletin* **136**, 673–688 (2024).
33. Laurent, O., Moyen, J.-F., Wotzlaw, J.-F., Björnsen, J. & Bachmann, O. Early Earth zircons formed in residual granitic melts produced by tonalite differentiation. *Geology* **50**, 437–441 (2022).
34. Hughes, J. M. & Rakovan, J. F. Structurally robust, chemically diverse: apatite and apatite supergroup minerals. *Elements* **11**, 165–170 (2015).
35. Piccoli, P. M. & Candela, P. A. Apatite in igneous systems. *Rev. Mineral. Geochem.* **48**, 255–292 (2002).

36. Huang, G., Palin, R., Wang, D. & Guo, J. Open-system fractional melting of Archean basalts: implications for tonalite–trondhjemite–granodiorite (TTG) magma genesis. *Contrib. Mineral. Petrol.* **175**, 102 (2020).

37. Hernández-Montenegro, J. D., Palin, R. M., Zuluaga, C. A. & Hernández-Uribe, D. Archean continental crust formed by magma hybridization and voluminous partial melting. *Sci. Rep.* **11**, 5263 (2021).

38. O'Neill, H. S. C. The smoothness and shapes of chondrite-normalized rare earth element patterns in basalts. *J. Petrol.* **57**, 1463–1508 (2016).

39. Gao, Y., O'Neill, H. S. C. & Mavrogenes, J. A. Garnet versus amphibole: Implications for magmatic differentiation and slab melting. *Geology* **52**, 125–129 (2024).

40. Tatnell, L., Anenburg, M. & Loucks, R. Porphyry copper deposit formation: identifying garnet and amphibole fractionation with REE pattern curvature modeling. *Geophys. Res. Lett.* **50**, e2023GL103525 (2023).

41. Xiang, H. & Connolly, J. A. GeoPS: An interactive visual computing tool for thermodynamic modelling of phase equilibria. *J. Metamorph. Geol.* **40**, 243–255 (2022).

42. Alonso-Perez, R., Müntener, O. & Ulmer, P. Igneous garnet and amphibole fractionation in the roots of island arcs: experimental constraints on andesitic liquids. *Contrib. Mineral. Petrol.* **157**, 541–558 (2009).

43. Smithies, R., Champion, D. & Van Kranendonk, M. Formation of Paleoarchean continental crust through infracrustal melting of enriched basalt. *Earth Planet. Sci. Lett.* **281**, 298–306 (2009).

44. Van Kranendonk, M. J. et al. Making it thick: a volcanic plateau origin of Palaeoarchean continental lithosphere of the Pilbara and Kaapvaal cratons. *Geol. Soc. Lond. Spec. Publ.* **389**, 83–111 (2015).

45. Kendall-Langley, L. A., Kemp, A. I., Hawkesworth, C. J., Hinton, E. J. C. C. T. R. & Roberts, M. P. Quantifying F and Cl concentrations in granitic melts from apatite inclusions in zircon. *Contrib. Mineral. Petrol.* **176**, 1–19 (2021).

46. Li, W., Chakraborty, S., Nagashima, K. & Costa, F. Multicomponent diffusion of F, Cl and OH in apatite with application to magma ascent rates. *Earth Planet. Sci. Lett.* **550**, 116545 (2020).

47. O'Sullivan, G., Chew, D., Kenny, G., Henrichs, I. & Mulligan, D. The trace element composition of apatite and its application to detrital provenance studies. *Earth Sci. Rev.* **201**, 103044 (2020).

48. Wang, H. et al. Apatite as a magma redox indicator and its application in metallogenic research. *Lithos* **422**, 106749 (2022).

49. Meng, X. et al. Formation of oxidized sulfur-rich magmas in Neoarchaean subduction zones. *Nat. Geosci.* **15**, 1064–1070 (2022).

50. Tripathi, P. et al. Amphibolite–granulite facies mid-crustal basement in Deccan Large Igneous Province and its implication on Precambrian crustal evolution: evidence from Killari borehole studies. *Int. J. Earth Sci.* **110**, 2661–2683 (2021).

51. Baker, D. R. & Alletti, M. Fluid saturation and volatile partitioning between melts and hydrous fluids in crustal magmatic systems: the contribution of experimental measurements and solubility models. *Earth Sci. Rev.* **114**, 298–324 (2012).

52. Plank, T., Kelley, K. A., Zimmer, M. M., Hauri, E. H. & Wallace, P. J. Why do mafic arc magmas contain~ 4wt% water on average?. *Earth Planet Sci. Lett.* **364**, 168–179 (2013).

53. Herzberg, C., Condie, K. & Korenaga, J. Thermal history of the Earth and its petrological expression. *Earth Planet Sci. Lett.* **292**, 79–88 (2010).

54. Hawkesworth, C. J., Cawood, P. A., Dhuime, B. & Kemp, T. I. Earth's continental lithosphere through time. *Annu. Rev. Earth Planet. Sci.* **45**, 169–198 (2017).

55. Burke, K. & Kidd, W. Were Archean continental geothermal gradients much steeper than those of today?. *Nature* **272**, 240–241 (1978).

56. Ptáček, M. P., Dauphas, N. & Greber, N. D. Chemical evolution of the continental crust from a data-driven inversion of terrigenous sediment compositions. *Earth Planet Sci. Lett.* **539**, 116090 (2020).

57. Brown, M. & Johnson, T. Secular change in metamorphism and the onset of global plate tectonics. *Am. Mineralogist* **103**, 181–196 (2018).

58. Hartnady, M. I. et al. Fluid processes in the early Earth and the growth of continents. *Earth Planet. Sci. Lett.* **594**, 117695 (2022).

59. Sobolev, A. V. et al. Deep hydrous mantle reservoir provides evidence for crustal recycling before 3.3 billion years ago. *Nature* **571**, 555–559 (2019).

60. Arndt, N. T. The formation and evolution of the continental crust. *Geochem. Perspect.* **2**, 405–405 (2013).

61. Nebel, O., Campbell, I. H., Sossi, P. A. & Van Kranendonk, M. J. Hafnium and iron isotopes in early Archean komatiites record a plume-driven convection cycle in the Hadean Earth. *Earth Planet Sci. Lett.* **397**, 111–120 (2014).

62. Zhang, Q., Zhu, D., Du, W. & Liu, Y. A model of crust–mantle differentiation for the early. *Earth. Acta Geochim.* **41**, 689–703 (2022).

63. Tamblyn, R. et al. Hydrated komatiites as a source of water for TTG formation in the Archean. *Earth Planet. Sci. Lett.* **603**, 117982 (2023).

64. Mai, V. V. & Korenaga, J. What controlled the thickness of continental crust in the Archean?. *Geology* **50**, 1091–1095 (2022).

65. Flament, N., Rey, P. F., Coltice, N., Dromart, G. & Olivier, N. Lower crustal flow kept Archean continental flood basalts at sea level. *Geology* **39**, 1159–1162 (2011).

66. Roman, A. & Arndt, N. Differentiated Archean oceanic crust: Its thermal structure, mechanical stability and a test of the sagduction hypothesis. *Geochim. Cosmochim. Acta* **278**, 65–77 (2020).

67. Stern, R. J. Subduction zones. *Rev. Geophys.* **40**, 3-1–3-38 (2002).

68. van Hunen, J. & van den Berg, A. P. Plate tectonics on the early Earth: limitations imposed by strength and buoyancy of subducted lithosphere. *Lithos* **103**, 217–235 (2008).

69. Sizova, E., Gerya, T., Brown, M. & Perchuk, L. Subduction styles in the Precambrian: insight from numerical experiments. *Lithos* **116**, 209–229 (2010).

70. Liu, C. T., Ye, C. Y. & ZhangZhou, J. Secular changes in the occurrence of subduction during the Archean. *Geophys. Res. Lett.* **51**, e2023GL107996 (2024).

71. Gutscher, M.-A., Maury, R. & Eissen, J.-P. & Bourdon, E. Can slab melting be caused by flat subduction?. *Geology* **28**, 535–538 (2000).

72. Martin, H. & Moyen, J.-F. Secular changes in tonalite-trondhjemite-granodiorite composition as markers of the progressive cooling of Earth. *Geology* **30**, 319–322 (2002).

73. Liu, S. et al. Archean crust-mantle geodynamic regimes: a review. *Geosyst. Geoenviron.* **1**, 100063 (2022).

74. Fischer, R. & Gerya, T. Regimes of subduction and lithospheric dynamics in the Precambrian: 3D thermomechanical modelling. *Gondwana Res.* **37**, 53–70 (2016).

75. Ganne, J. & Feng, X. Primary magmas and mantle temperatures through time. *Geochem. Geophys. Geosyst.* **18**, 872–888 (2017).

76. van Hunen, J. & Moyen, J.-F. Archean subduction: fact or fiction?. *Annu. Rev. Earth Planet. Sci.* **40**, 195–219 (2012).

77. Korenaga, J. Hadean geodynamics and the nature of early continental crust. *Precambrian Res.* **359**, 106178 (2021).

78. Huang, G., Mitchell, R. N., Palin, R. M., Spencer, C. J. & Guo, J. Barium content of Archaean continental crust reveals the onset of subduction was not global. *Nat. Commun.* **13**, 6553 (2022).

79. Sizova, E., Gerya, T. & Brown, M. Contrasting styles of Phanerozoic and Precambrian continental collision. *Gondwana Res.* **25**, 522–545 (2014).

80. Dhuime, B., Hawkesworth, C. J., Cawood, P. A. & Storey, C. D. A change in the geodynamics of continental growth 3 billion years ago. *Science* **335**, 1334–1336 (2012).

81. Laurent, O., Martin, H., Moyen, J.-F. & Doucelance, R. The diversity and evolution of late-Archean granitoids: Evidence for the onset of "modern-style" plate tectonics between 3.0 and 2.5 Ga. *Lithos* **205**, 208–235 (2014).

82. Veizer, J. & MacKenzie, F. T. Evolution of sedimentary rocks. *Treatise Geochem.* **7**, 239–407 (2003).

83. Cawood, P. A. et al. Geological archive of the onset of plate tectonics. *Philos. Trans. R. Soc. A Math. Phys. Eng. Sci.* **376**, 20170405 (2018).

84. Palin, R. M. et al. Secular change and the onset of plate tectonics on Earth. *Earth Sci. Rev.* **207**, 103172 (2020).

85. Sun, G. et al. Thermal state and evolving geodynamic regimes of the Meso-to Neoarchean North China Craton. *Nat. Commun.* **12**, 3888 (2021).

86. Holland, T. & Powell, R. An improved and extended internally consistent thermodynamic dataset for phases of petrological interest, involving a new equation of state for solids. *J. Metamorph. Geol.* **29**, 333–383 (2011).

87. Green, E. et al. Activity–composition relations for the calculation of partial melting equilibria in metabasic rocks. *J. Metamorph. Geol.* **34**, 845–869 (2016).

88. White, R. W., Powell, R., Holland, T., Johnson, T. & Green, E. New mineral activity–composition relations for thermodynamic calculations in metapelitic systems. *J. Metamorph. Geol.* **32**, 261–286 (2014).

89. Holland, T. & Powell, R. Activity–composition relations for phases in petrological calculations: an asymmetric multicomponent formulation. *Contrib. Mineral. Petrol.* **145**, 492–501 (2003).

90. White, R., Powell, R., Holland, T. & Worley, B. The effect of TiO_2 and Fe_2O_3 on metapelitic assemblages at greenschist and amphibolite facies conditions: mineral equilibria calculations in the system K_2O-FeO-MgO-Al_2O_3-SiO_2-H_2O-TiO_2-Fe_2O_3. *J. Metamorph. Geol*. **18**, 497–511 (2000).

91. White, R., Powell, R. & Clarke, G. The interpretation of reaction textures in Fe-rich metapelitic granulites of the Musgrave Block, central Australia: constraints from mineral equilibria calculations in the system K2O–FeO–MgO–Al2O3–SiO2–H2O–TiO2–Fe2O3. *J. Metamorph. Geol.* **20**, 41–55 (2002).

92. Gao, L. et al. Oxidation of Archean upper mantle caused by crustal recycling. *Nat. Commun.* **13**, 3283 (2022).

93. Boehnke, P., Watson, E. B., Trail, D., Harrison, T. M. & Schmitt, A. K. Zircon saturation re-revisited. *Chem. Geol.* **351**, 324–334 (2013).

94. Harrison, T. M. & Watson, E. B. The behavior of apatite during crustal anatexis: equilibrium and kinetic considerations. *Geochim. Cosmochim. Acta* **48**, 1467–1477 (1984).

95. Bédard, J. H. A catalytic delamination-driven model for coupled genesis of Archaean crust and sub-continental lithospheric mantle. *Geochim. Cosmochim. Acta* **70**, 1188–1214 (2006).

96. Xiong, X. et al. Partitioning of Nb and Ta between rutile and felsic melt and the fractionation of Nb/Ta during partial melting of hydrous metabasalt. *Geochim. Cosmochim. Acta* **75**, 1673–1692 (2011).

97. Anenburg, M. & Williams, M. J. Quantifying the tetrad effect, shape components, and Ce–Eu–Gd anomalies in rare earth element patterns. *Math. Geosci.* **54**, 47–70 (2022).

98. Sotiriou, P., Polat, A., Windley, B. & Kusky, T. Temporal variations in the incompatible trace element systematics of Archean TTGs: implications for crustal growth and tectonic processes in the early Earth. *Earth Sci. Rev.* **236**, 104274 (2023).

99. Ge, R. et al. Generation of Eoarchean continental crust from altered mafic rocks derived from a chondritic mantle: The~ 3.72 Ga Aktash gneisses, Tarim Craton (NW China). *Earth Planet. Sci. Lett.* **538**, 116225 (2020).

100. Johnson, T. et al. Secular change in TTG compositions: Implications for the evolution of Archaean geodynamics. *Earth Planet. Sci. Lett.* **505**, 65–75 (2019).

101. Jenner, F. et al. Evidence for subduction at 3.8 Ga: geochemistry of arc-like metabasalts from the southern edge of the Isua Supracrustal Belt. *Chem. Geol.* **261**, 83–98 (2009).

102. Kaczmarek, M.-A., Reddy, S. M., Nutman, A. P., Friend, C. R. & Bennett, V. C. Earth's oldest mantle fabrics indicate Eoarchaean subduction. *Nat. Commun.* **7**, 10665 (2016).

103. Polat, A., Hofmann, A. & Rosing, M. T. Boninite-like volcanic rocks in the 3.7–3.8 Ga Isua greenstone belt, West Greenland: geochemical evidence for intra-oceanic subduction zone processes in the early Earth. *Chem. Geol.* **184**, 231–254 (2002).

104. Stock, M. J. et al. Tracking volatile behaviour in sub-volcanic plumbing systems using apatite and glass: insights into pre-eruptive processes at Campi Flegrei, Italy. *J. Petrol.* **59**, 2463–2492 (2018).

105. Antoine, C., Bruand, E., Guitreau, M. & Devidal, J. L. Understanding preservation of primary signatures in apatite by comparing matrix and zircon-hosted crystals from the Eoarchean Acasta Gneiss Complex (Canada). *Geochem., Geophysics, Geosystems* **21**, e2020GC008923 (2020).

106. Madon, B., Mathieu, L. & Marsh, J. H. Oxygen fugacity and volatile content of syntectonic magmatism in the Neoarchean Abitibi greenstone belt, Superior Province, Canada. *Minerals* **10**, 966 (2020).

107. Gillespie, J. et al. Isotopic modelling of Archean crustal evolution from comagmatic zircon–apatite pairs. *Earth Planet Sc. Lett.* **575**, 117194 (2021).

108. Guo, J. et al. Archean trondhjemitic crust at depth in Yangtze Craton: evidence from TTG xenolith in mafic dyke and apatite inclusion pressure in zircon. *Precambrian Res.* **354**, 106055 (2021).

109. Meng, X. et al. Variable modes of formation for tonalite–trondhjemite–granodiorite–diorite (TTG)-related porphyry-type Cu±Au deposits in the Neoarchean southern Abitibi subprovince (Canada): evidence from petrochronology and oxybarometry. *J. Petrol.* **62**, egab079 (2021).

110. Tang, M., Chen, H., Song, S., Sun, G. & Wang, C. Zircon Eu/Eu* in Archean TTGs with implications for the role of endogenic oxidation in Archean crustal differentiation. *Geochim. Cosmochim. Acta* **378**, 259–269 (2024).

111. Li, H. & Hermann, J. Chlorine and fluorine partitioning between apatite and sediment melt at 2.5GPa, 800C: A new experimentally derived thermodynamic model. *Am. Mineralogist* **102**, 580–594 (2017).

112. Riker, J., Humphreys, M. C., Brooker, R. A., De Hoog, J. C. & EIMF First measurements of OH-C exchange and temperature-dependent partitioning of OH and halogens in the system apatite–silicate melt. *Am. Mineralogist* **103**, 260–270 (2018).

113. Li, W., Costa, F. & Nagashima, K. Apatite crystals reveal melt volatile budgets and magma storage depths at Merapi volcano, Indonesia. *J. Petrol.* **62**, egaa100 (2021).

114. Dalou, C., Le Losq, C., Mysen, B. O. & Cody, G. D. Solubility and solution mechanisms of chlorine and fluorine in aluminosilicate melts at high pressure and high temperature. *Am. Mineralogist* **100**, 2272–2283 (2015).

115. Aiuppa, A., Baker, D. & Webster, J. Halogens in volcanic systems. *Chem. Geol.* **263**, 1–18 (2009).

116. Liu, H., Sun, W. -d & Deng, J.-H. Transition of subduction-related magmatism from slab melting to dehydration at 2.5 Ga. *Precambrian Res.* **337**, 105524 (2020).

Acknowledgements

Author contributions

Hairuo Wang: Investigation, Formal analysis, Thermodynamic-geochemical modelling, Visualization, Writing—original draft, Writing—review & editing. Keda Cai: Conceptualization, Writing—review & editing, Funding acquisition. Min Sun: Writing—review & editing. Wei-ran Li: Writing—review & editing. Ming Chen: Writing—review & editing, Funding acquisition. Xiao-ping Xia: Writing—review & editing.

Competing interests

The authors declare no competing interests.

Additional information

Supplementary information The online version contains supplementary material available at https://doi.org/10.1038/s43247-025-02973-z.

Correspondence and requests for materials should be addressed to Keda Cai.